



**HAL**  
open science

## Experimental Phase-equilibrium Constraints on the Phonolite Magmatic System of Erebus Volcano, Antarctica

Yves Moussallam, Clive Oppenheimer, Bruno Scaillet, Philip R. Kyle

► **To cite this version:**

Yves Moussallam, Clive Oppenheimer, Bruno Scaillet, Philip R. Kyle. Experimental Phase-equilibrium Constraints on the Phonolite Magmatic System of Erebus Volcano, Antarctica. *Journal of Petrology*, 2013, 54 (7), pp.1285-1307. 10.1093/petrology/egt012 . insu-00813668

**HAL Id: insu-00813668**

**<https://insu.hal.science/insu-00813668>**

Submitted on 4 May 2014

**HAL** is a multi-disciplinary open access archive for the deposit and dissemination of scientific research documents, whether they are published or not. The documents may come from teaching and research institutions in France or abroad, or from public or private research centers.

L'archive ouverte pluridisciplinaire **HAL**, est destinée au dépôt et à la diffusion de documents scientifiques de niveau recherche, publiés ou non, émanant des établissements d'enseignement et de recherche français ou étrangers, des laboratoires publics ou privés.



Distributed under a Creative Commons Attribution - NonCommercial - NoDerivatives 4.0  
International License

# Experimental Phase-equilibrium Constraints on the Phonolite Magmatic System of Erebus Volcano, Antarctica

1. Yves Moussallam<sup>1\*</sup>
2. Clive Oppenheimer<sup>1</sup>
3. Bruno Scaillet<sup>2</sup> and
4. Philip R. Kyle<sup>3</sup>

<sup>1</sup>*Department of Geography, University of Cambridge, Downing Place, Cambridge CB2 3EN, UK*

<sup>2</sup>*Institut des Sciences de la Terre d'Orléans, Université D'Orléans–CNRS–BRGM, 1A RUE DE LA Férollerie, 45071 Orléans Cedex 2, France*

<sup>3</sup>*Department of Earth and Environmental Science, New Mexico Institute of Mining and Technology, 801 Leroy Place, Socorro, NM 87801, USA*

## Abstract

Field observations and petrological studies have recently advanced understanding of the magmatic system of Erebus volcano, renowned for its sustained CO<sub>2</sub>-rich degassing, and long-lived phonolitic lava lake. However, this body of work has highlighted uncertainty in several key parameters, including the magma temperature, redox state and the depth of the reservoir presumed to maintain the lava lake. Here, we use experimentally determined phase equilibria to constrain these unknowns. The experiments ranged in temperature from 900 to 1025°C, in pressure from atmospheric to 300 MPa, in water content from 0 to 8 wt %, and in oxygen fugacity from NNO + 4 (where NNO is nickel–nickel oxide) to QFM – 2 (where QFM is quartz–fayalite–magnetite). The natural system was experimentally reproduced at 950 ± 25°C, a pressure below 200 MPa, redox conditions between QFM and QFM – 1, and remarkably low water contents of less than 0.5 wt %. These findings help in understanding petrological observations, including melt inclusion data, as well as the measured composition of gas emissions from the lava lake. Biotite and amphibole appear in the crystallization sequence at around 925°C, even under very dry conditions (biotite). Both biotite and amphibole are absent in the phonolites erupted over the last 20 kyr at Erebus. The constant abundance of anorthoclase observed in the erupted lavas and bombs indicates that the shallow magmatic system feeding the Erebus lava lake (below pressures of 200 MPa) has been thermally buffered at 950 ± 25°C over this time period, possibly reflecting steady-state connection with the deep feeding system rooted in the mantle. Combined with recent seismological data, our results suggest that if a large phonolitic reservoir exists, then it should lie in the depth range 4–7.5 km. The tight constraints on temperature and redox conditions will be valuable for future thermodynamical and rheological modelling.

**Key words** : Erebus ; phonolite ; phase equilibrium ; lava lake ; CO<sub>2</sub> ; degassing

## Introduction

Erebus represents an archetype of an open-vent volcano, with the uppermost part of its magmatic conduit exposed at the surface as an active lava lake. A conceptual model has been

proposed to explain the persistence of the convecting lava lake, with the lake connected to a source reservoir via a narrow (<10 m radius) conduit in which there is a counter flow of denser degassed magma and buoyant, volatile-rich and un-degassed magma (Calkins *et al.*, 2008; Oppenheimer *et al.*, 2009). Numerical models of magma convection in the conduit and its relationship with the lava lake have been described by Molina *et al.* (2012); conceptual models of such behaviour date back further (e.g. Francis *et al.*, 1993; Kazahaya *et al.*, 1994). Such models, however, still require validation from field-based observations and experimental studies. Magma temperature and reservoir depth are two crucial parameters required to understand the system and for the further development of modelling endeavours.

The first estimate of lava temperature at Erebus was made by training an optical pyrometer on incandescent cracks in the lava lake (viewed from the crater rim), and suggested a magma temperature of  $\sim 1000^{\circ}\text{C}$  (Kyle, 1977). This is consistent with olivine–clinopyroxene thermometry (Caldwell & Kyle, 1994) and was also found to be the temperature at which anorthoclase-hosted melt inclusions in Erebus phonolite anneal during heating stage measurements at 0.10 MPa (Dunbar *et al.*, 1994). The only other field-based measurement indicates a minimum temperature of  $923^{\circ}\text{C}$ , using mid-infrared imaging with a hand-held thermal camera operated from the crater rim (Calkins *et al.*, 2008). More recently, thermodynamic calculations based on measurements of CO, CO<sub>2</sub>, SO<sub>2</sub> and OCS in the gases emitted from the lava lake have suggested an equilibrium gas temperature of  $1080^{\circ}\text{C}$  (Burgisser *et al.*, 2012).

The second significant unknown is the depth of the hypothesized magma chamber that feeds the lava lake. Oppenheimer *et al.* (2011) modelled anorthoclase-hosted melt inclusion CO<sub>2</sub> and H<sub>2</sub>O abundances and computed degassing paths to the surface to suggest that phonolite is present from depths of  $\sim 10$  km up to the surface, but this hardly constrains the location of any suspected magma reservoir feeding the summit lava lake. Seismic illumination from Strombolian eruption coda and active source tomography experiments were used to image the subsurface in the summit region (<4 km depth below the surface; Chaput *et al.*, 2012; Zandomenighi *et al.*, 2013), revealing a complex shallow plumbing system but no large single reservoir.

Here, we use an experimental approach to constrain the nature of the shallow plumbing system of Erebus in terms of pressure–temperature–volatile space. Our experimental strategy is two-fold: the first step consists of exploring lava lake conditions using an Erebus lava bomb as starting material, and spanning a temperature range from  $1025^{\circ}\text{C}$  to  $905^{\circ}\text{C}$  at an oxygen fugacity ( $f\text{O}_2$ ) imposed by a controlled atmosphere with a CO<sub>2</sub>/CO ratio of 15 mol mol<sup>-1</sup> (corresponding to  $\sim \text{QFM} - 0.7$  to  $\text{QFM} - 1$ ; where QFM refers to the quartz–fayalite–magnetite solid buffer in log units). The second set of experiments uses the same natural sample as starting material but explores the pressure range from 20 to 300 MPa, at temperatures between 900 and  $1000^{\circ}\text{C}$  and oxygen fugacity from  $\text{QFM} - 2$  to  $\text{NNO} + 4$  (NNO referring to the Ni–NiO solid buffer, which is  $\sim 0.7$  log units of  $f\text{O}_2$  more oxidized than QFM).

## Volcanological background

Erebus, the southernmost active volcano in the world ( $3794$  m,  $77.58^{\circ}\text{S}$ ,  $161.17^{\circ}\text{E}$ ), is a composite intraplate stratovolcano located on Ross Island, Antarctica (Fig. 1a). It belongs to the Erebus volcanic province, which constitutes part of the McMurdo Volcanic Group (Kyle, 1990a, 1990b; Kyle *et al.*, 1992). The regional volcanism is related to rifting of the western

margin of the Ross Embayment (part of the West Antarctic Rift System) and a hypothesized mantle plume (Kyle *et al.*, 1992). P-wave tomography reveals a low-velocity anomaly extending to ~400 km depth, providing some evidence for such a plume (Gupta *et al.*, 2009).

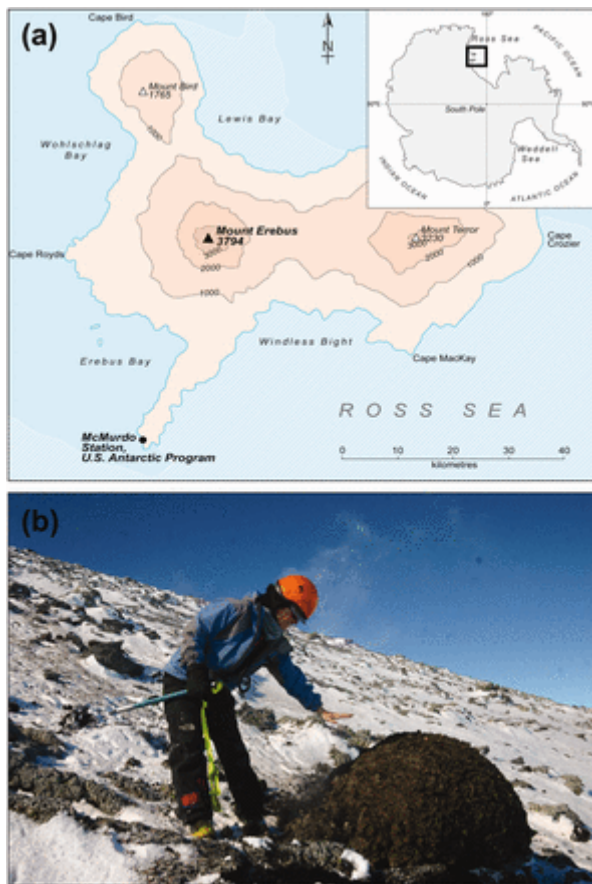


Fig. 1 : (a) Location map of Erebus volcano on Ross Island. Inset shows the location of Ross Island within the Antarctic continent. (b) A freshly erupted volcanic bomb on the flank of Erebus volcano, December 2005.

The first of three stages of eruptive activity at Erebus volcano began ~1.3 Myr ago (Esser *et al.*, 2004). These three stages have been documented by repeated  $^{40}\text{Ar}/^{39}\text{Ar}$  dating campaigns (Esser *et al.*, 2004; Harpel *et al.*, 2004, 2008; Kelly *et al.*, 2008a) and consist of an initial shield-building phase with eruption of basanite (1.3–1.0 Ma), followed by a cone-building phase dominated by phonotephrites, later partially destroyed by a caldera collapse event (~750 kyr ago), and finally the construction of the modern Erebus cone by anorthoclase-phyric tephriphonolite and phonolite lavas, starting 250 kyr ago and continuing to the present (Kelly *et al.*, 2008a).

Acknowledging the long gaps in field observations, the present volcanic activity appears to have persisted since Erebus volcano was first witnessed and described by James Clark Ross in 1841. The active lava lake sits in the Inner Crater of the Main Crater at the volcano's summit (Kyle *et al.*, 1982, 1994; Oppenheimer *et al.*, 2009). The lava lake is sporadically disturbed by Strombolian eruptions associated with the rupture of large  $\text{CO}_2$ -rich gas slugs at the lake surface (Aster *et al.*, 2008; Gerst *et al.*, 2008, 2013; Oppenheimer *et al.*, 2011). Some of these

explosions are large enough to expel all the lava in the lake and eject bombs onto the crater rim, where they can be collected for petrological studies (Kelly *et al.*, 2008b).

## Experimental Methods

### Starting material

The starting material (ERE 97018) is a phonolitic bomb erupted in 1997 and collected on the crater rim. The ambient air and ground temperature ensured rapid quenching (Fig. 1b). This particular sample was used because of the large sample size (5 kg), which was jaw crushed and ground to a fine (5–10  $\mu\text{m}$ ) homogeneous powder with a tungsten carbide swing mill (Eschenbacher, 1998). The large amount of homogenized sample powder provides reasonable assurance that the measured bulk-rock composition is representative of the magma composition, minimizing the effect of the abundant anorthoclase megacrysts (typically a few centimetres in length).

Table 1 summarizes previous glass and whole-rock analyses of the sample from Eschenbacher (1998) together with representative analyses of minerals present in Erebus bombs erupted over the last 30 years (Kelly *et al.*, 2008b). The bombs are of phonolitic composition based on the total alkalis–silica (TAS) classification (Le Bas *et al.*, 1986). The natural modal phase proportion is 65.5% matrix glass, 30.6% anorthoclase feldspar, 1.7% titanomagnetite, 1.3% olivine, 0.4% clinopyroxene and 0.6% fluorapatite (Kelly *et al.*, 2008b). Phonolite lava bombs are highly vesicular and display an extreme phaneritic texture with anorthoclase crystals up to around 7 cm in length. The groundmass is mostly glassy, essentially microlite free, and contains small amounts of olivine, opaque oxides, clinopyroxene, and fluorapatite. The clinopyroxenes in some bombs can be up to 1 cm in length. Using a single sample as starting material for both 1 atmosphere (0.10 MPa) and pressurized experiments to re-create the lava lake and the reservoir is justified as the composition of phonolite erupted in the last 20 kyr at Erebus is virtually constant, and both bombs erupted from the lava lake and large lava flows on the volcano flanks have exactly the same mineral assemblage (Kelly *et al.*, 2008b). This implies that the natural phase assemblage is at equilibrium both in the reservoir and in the lava lake.

Table 1 : Electron microprobe analysis (wt %) of bomb sample ERE 97018 erupted from Erebus volcano and used in the experimental studies

	SM		WR		MG		OL		CPX		Anorth	Ti-mt		F-ap	
<i>n</i> :	15	SD	2	SD	18	SD	67	SD	19	SD	755	643	SD	63	SD
SiO <sub>2</sub>	56.05	0.33	56.23	0.26	55.11	0.60	34.80	-0.43	50.89	-0.3	62.87			0.35	-0.1
TiO <sub>2</sub>	0.96	0.04	0.99	0.01	1.03	0.03			1.35	-0.25		24.52	-0.51		
Al <sub>2</sub> O <sub>3</sub>	19.22	0.27	19.82	0.13	19.85	0.31	0.01	-0.01	2.81	-0.12	22.81	2.27	-0.17		
FeO <sub>T</sub>	5.24	0.18	5.35	0.01	5.34	0.07	38.33	-0.6	9.54	-0.16	0.19	67.87	-1.36	0.51	-0.45
MnO	0.23	0.08	0.23	0.00	0.27	0.06	2.45	-0.15	0.65	-0.03		1.76	-0.11	0.11	-0.05
MgO	0.91	0.03	0.88	0.01	0.83	0.03	23.53	-0.33	12.23	-0.2		2.89	-0.08		
CaO	2.60	0.07	2.68	0.01	1.88	0.08	0.50	-0.09	21.13	-0.33	3.36			53.67	-0.98
Na <sub>2</sub> O	7.90	0.28	8.38	0.01	9.07	0.19			0.93	-0.08	7.57			0.12	-0.05
K <sub>2</sub> O	4.56	0.11	4.51	0.05	5.65	0.05					3.12				
P <sub>2</sub> O <sub>5</sub>	0.40	0.07	0.42	0.00	0.30	0.04								41.07	-0.88
Total	98.09		99.61		99.33		99.62		99.53		99.92	99.31		95.83	

SM, starting material; WR, whole-rock; MG, matrix glass; OL, olivine; CPX, clinopyroxene; Anorth, anorthoclase; Ti-mt, titanomagnetite; F-ap, fluorapatite. Glass and whole-rock analyses are from Eschenbacher (1998). Representative analyses of olivine, clinopyroxene, anorthoclase, titanomagnetite and fluorapatite in lava bombs erupted from Erebus volcano between December 1972 and January 2004 are from Kelly *et al.* (2008b). F content of apatite is 3.06 wt %.

Powder (10 g) from sample ERE 97018 was dried at 140°C overnight, then placed in a platinum crucible, heated at 1400°C in a 1 atmosphere (0.1 MPa) furnace for 2 h, and then quenched. The glass retrieved was pulverized (in an agate grinder) to a fine powder and heated once more under the same conditions for an additional 2 h. The highly oxidizing conditions (open atmosphere) minimize the amount of Fe loss to the crucible, and convert most of the iron to Fe<sup>3+</sup>. After quenching (in water at room temperature) the glass was imaged by scanning electron microscope (SEM) to verify the absence of crystals. Subsequent analysis by electron microprobe also confirmed the homogeneity of the glass (Table 1) and confirmed that no Fe loss, and only minimal Na loss, had occurred. This starting glass was finely ground and used for all experiments.

#### Controlled-atmosphere furnace at 1 atmosphere

To re-create the magmatic conditions of the lava lake we used a controlled-atmosphere furnace at the Department of Earth Sciences, University of Cambridge. The furnace operates at atmospheric pressure (0.1 MPa) and is heated by a silicon carbide resistance wire wrapped around an aluminium cylinder. The current is controlled by a Eurotherm 2404 series regulator able to maintain a constant temperature ( $\pm 2^\circ\text{C}$ ) within the furnace. The cooling system consists of a constant flow of water circulating within the furnace.

For each experiment, 50 mg of sample was mixed with a liquid glue (UHU brand ‘twist and glue’) and placed on a thin platinum wire tied to two thicker platinum wires located at the end of a ceramic can (sample holder). The sample was then introduced in the furnace and heated to the required temperature. During heating the glue evaporates leaving the sample on the thin

platinum wire. The sample temperature was monitored continuously by a thermocouple located 1 cm from the sample. A controlled mixture of CO and CO<sub>2</sub> gases was circulated through the furnace and monitored during the experiments by calibrated flow meters. At the end of each experiment, the sample was dropped and quenched in a container of deionized water, so as to preserve the chemical and textural equilibrium attained. The drop was initiated by short-circuiting the thin platinum wire by passing a current through the thick platinum wires. To minimize Fe loss to the Pt wire (forming Fe–Pt alloy), all Pt wires were pre-saturated with iron. Sample powder was pasted on each wire, melted at 1200°C under reduced conditions [ $\log(f\text{O}_2) = -9.6$ ;  $\Delta\text{QFM} = -1.4$ ] and left to equilibrate for 2 days. The wires were then placed in hydrofluoric acid to dissolve any adhering glass and only then used for the phase-equilibrium experiments. After each experiment, the charge with its platinum wire was embedded in epoxy resin and polished for SEM and microprobe analysis.

Seven equilibrium experiments were carried out covering a temperature range from 905 to 1025°C. All experiments lasted about 4 days and the gas flux was maintained at a CO<sub>2</sub>/CO ratio of 15 mol mol<sup>-1</sup> [ $\log(f\text{O}_2)$ , equivalent to QFM – 0.7 to QFM – 1]. This gas ratio was used as it is typical of the ratio measured for emissions from the lava lake by open-path Fourier transform infrared (FTIR) spectroscopy (Oppenheimer & Kyle, 2008; Oppenheimer *et al.*, 2009, 2011). The stable CO<sub>2</sub>/CO ratio observed in the gas emission, the abundance of hydrogen detected in the gas and aerosol plume when it reaches the crater rim (Moussallam *et al.*, 2012), and their compatibility with redox conditions computed for the lava lake from mineral compositional data provide very strong evidence that the magmatic gas is effectively quenched on sudden cooling in the atmosphere (in thermodynamical terms, the CO<sub>2</sub>/CO and H<sub>2</sub>O/H<sub>2</sub> contents of the plume are far from equilibrium in air).

#### Internally heated pressure vessels

To investigate the phonolite magmatic system that feeds the lava lake, we performed a series of phase-equilibrium experiments at a range of pressures (20–300 MPa), temperatures (900–1000°C) and  $X_{\text{H}_2\text{O}}$  (mole fraction of water in the fluid phase, from near zero to unity) under reduced conditions ( $f\text{O}_2 \approx \text{QFM}$  or below).

We used internally heated pressure vessels at the ISTO–CNRS laboratory in Orléans, which can reach pressures of up to 400 MPa under controlled temperature (up to 1200°C) and oxygen fugacity conditions. The vessel was pressurized using an argon–hydrogen gas mixture as the pressure medium to control redox state (Scaillet *et al.*, 1992). Heating was applied by a double-wound molybdenum furnace creating a stable ‘hot-spot’ zone. Two S-type thermocouples located on either side of this 5 cm wide ‘hot-spot’ permitted precise control of the heating resistances, thus preventing the establishment of thermal gradients.

Experimental charges consisted of natural anhydrous sample powder (30 mg) with  $X_{\text{H}_2\text{O}}$  loaded [the mole fraction of H<sub>2</sub>O added to the capsule, H<sub>2</sub>O/(H<sub>2</sub>O + CO<sub>2</sub>)] varying from zero to unity (i.e. pure CO<sub>2</sub> to pure H<sub>2</sub>O), which was loaded in gold capsules (2 cm in length, 2.5 mm inner diameter and 2.9 mm outer diameter). CO<sub>2</sub> was added to the capsule contents in the form of silver oxalate. The capsules were wrapped in liquid nitrogen-soaked tissue to prevent water loss and welded shut. For each experiment, six capsules and a sensor were placed in a sample holder hung by a thin Pt wire. The temperature gradient along the ‘hot-spot’ zone where the capsules were located was always <2°C. Rapid quenching was ensured by passing an electrical current to the holding Pt wire (Di Carlo *et al.*, 2006), so that the sample dropped into the cold part of the vessel, providing a cooling rate of >100°C s<sup>-1</sup>. The redox state was

measured *in situ* by a cobalt–cobalt oxide redox sensor (Taylor *et al.*, 1992; Di Carlo *et al.*, 2006) placed with the capsules in the sample holder during each experiment. After each experiment, the capsules were weighed to verify that no leakage had occurred. They were then opened and part of the charge (as a single fragment) was embedded in epoxy resin and polished for SEM and microprobe analysis.

We conducted a total of 66 phase-equilibrium experiments. The strategy was to produce a complete isobaric section at 100 MPa, in the temperature interval 900–1000°C. We then varied the pressure from 20 to 300 MPa at a magmatic temperature of 950°C as inferred from the isobaric experiments. Most experiments were performed at oxygen fugacity conditions close to the QFM buffer, or below. A subset of experiments were conducted under oxidized condition  $\log(fO_2) = \text{NNO} + 4]$  to evaluate the effect of oxygen fugacity on phase equilibria and compositions, in particular in the liquid. We chose the QFM buffer as the value for oxygen fugacity based on gas measurements made at the crater rim by Oppenheimer *et al.* (2011), who reported redox conditions ranging from NNO (for gases associated with Strombolian eruptions) to QFM – 1 (for passive degassing). These measurements together with chemical modelling (Burgisser *et al.*, 2012) suggest more oxidizing conditions at depth.

## Analytical Techniques

All experimental products were first examined by reflected light optical microscope and then by SEM. The SEM imaging ensured homogeneity in terms of phase distribution, and high-quality images were obtained to estimate modal proportions. All phases present were determined by semi-quantitative energy-dispersive spectroscopy. Detailed image analyses using the ImageJ freeware (<http://rsbweb.nih.gov/ij/>) were performed to estimate the modal proportion of each phase. Although most phases were easy to threshold from the SEM image and therefore yield a good estimate of their modal abundance, feldspars were often harder to differentiate from the background owing to the similarity of their composition to the glass. We therefore developed a technique to calculate the proportion of feldspar using a fuzzy algorithm for contrast enhancement, which was better able to distinguish the feldspar from the surrounding glass. Subsequently we used an outlier removal algorithm to suppress noise (mostly misclassified pixels within feldspar). The feldspar modal proportion was then calculated by thresholding in a similar way to that used for the other phases.

A series of 12 experimental supra-liquidus charges run at 1000°C in the pressure range 50–100 MPa produced crystal-free glass and were used as internal standards. The water concentrations of seven of them were determined by FTIR spectroscopy using a Nicolet 6700 spectrometer at ISTO–CNRS, equipped with an infrared microscope (type A590) and an MCT detector. Absorption spectra were acquired with 128 scans in the near-infrared region at a resolution of 4 cm<sup>-1</sup>. Samples were doubly polished and five measurement spots were analysed on each one to confirm the homogeneity of the water content in the glass. The total amount of water was obtained by the sum of the hydroxyl and molecular water concentrations calculated using the Beer–Lambert law, based on measurements of the 4470 cm<sup>-1</sup> and 5210 cm<sup>-1</sup> absorption bands. The sample thickness was measured on the infrared microscope and absorption peak heights were measured using a linear background correction. We used molar absorptivity values for phonolite from Carroll & Blank (1997) of 1.25 and 1.1 L mol<sup>-1</sup> cm<sup>-1</sup> for the 4470 and 5210 cm<sup>-1</sup> bands, respectively.

Electron microprobe analyses were performed using a Cameca SX100 at the Department of Earth Sciences, University of Cambridge. For glass analyses we used an accelerating voltage of 15 kV, a beam current of 2 nA and a defocused beam of 10  $\mu\text{m}$  whereas for mineral phases we used an accelerating voltage of 10 kV, a beam current of 6 nA and a focused beam of 1  $\mu\text{m}$  (details can be found in the Supplementary Data files DR2 and DR3, available for downloading at <http://www.petrology.oxfordjournals.org>). Na and K were analysed first to minimize alkali loss during analysis. Cobalt–cobalt oxide redox sensors were analysed on a Cameca SX50 at ISTO–CNRS using an accelerating voltage of 15 kV, a beam current of 20 nA and a focused beam. The water content of the glass from crystal-bearing charges was estimated using the by-difference method (Devine *et al.*, 1995). The difference from 100% of the microprobe analyses was calibrated against the  $\text{H}_2\text{O}$  from the glass standards previously described and analysed together with the crystal-bearing charges during each microprobe session.

## Results

All experimental charges are characterized by a homogeneous distribution of phases except for runs 97018\_C\_ATM\_05 and 97018\_C\_ATM\_06, in which fluorapatite accumulated locally. Attainment of equilibrium is attested to by the euhedral shape of all crystal phases (e.g. Berndt *et al.*, 2001), and geochemical criteria (i.e. homogeneous phase compositions, Fe/Mg partition between clinopyroxene and liquid; see below), and reflects the long duration of the experimental runs. In addition to glass and bubbles, the experimental phases identified are anorthoclase feldspar, clinopyroxene, amphibole, biotite, olivine, titanomagnetite and fluorapatite.

### 1 atmosphere phase equilibria and phase proportions

Results from the phase-equilibrium experiments at atmospheric pressure are summarized in Table 2 and illustrated in Fig. 2. At 0.1 MPa and near QFM – 0.9, the first phases to crystallize were fluorapatite and titanomagnetite, with liquidus temperatures higher than 1025°C (Table 2). Between 1000 and 1018°C anorthoclase crystallizes followed by clinopyroxene at 975 and 1000°C. Decreasing temperature further increases crystallinity, the system reaching nearly 90 wt % crystallization at around 900°C (Table 2). The latter feature indicates that the dry solidus of the Erebus phonolite is close to the lowest temperature investigated, considering in particular that crystallization is hindered by the relatively slow crystallization kinetics prevailing under  $\text{H}_2\text{O}$ -poor conditions (i.e. the amounts of crystallization under dry conditions should be considered as minima, particularly at low temperatures). The modal composition of the natural sample is closely re-created at 950°C and 975°C, except for olivine, which could not be detected in any of the 0.1 MPa experimental run products.

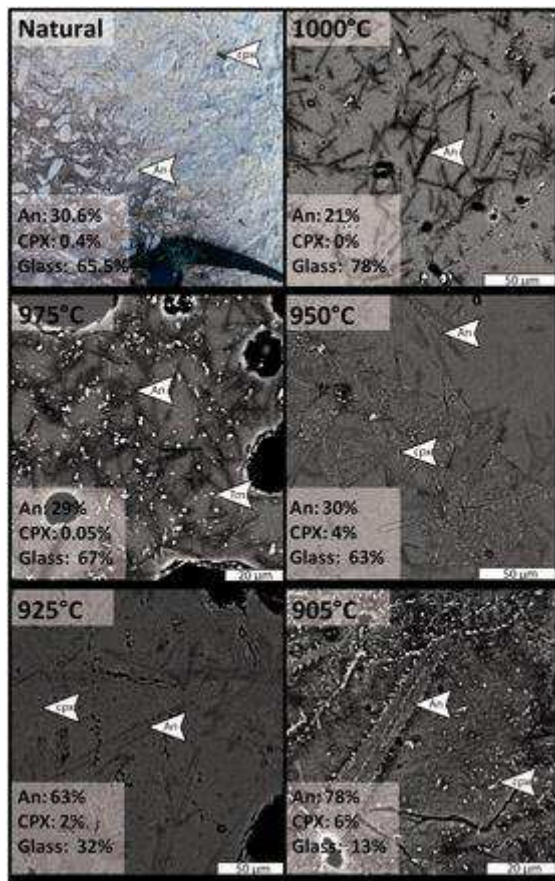


Fig. 2 : Photograph of natural Erebus lava and SEM photomicrographs showing the result of experiments at 1 atmosphere (0.1 MPa). The upper left photograph shows the weathered surface of a lava flow on Erebus, revealing the mineralogy at the macro-scale. Anorthoclase crystals appear light grey and clinopyroxenes are black. The head of an ice-axe is shown for scale and is about 20 cm long. Modal mineralogy is from Kelly *et al.* (2008b). All other photomicrographs are from experiments C-ATM 01 to 04 and 07. (Note the change in scale between images.) Anorthoclase crystals appear as dark elongated features in higher-temperature experiments (at 1000 and 975°C) and in lighter shades of grey surrounded by darker rims in lower-temperature experiments (950–905°C). An, anorthoclase; CPX, clinopyroxene; Tm, titanomagnetite.

Table 2 : Conditions and modal mineralogy of experiments conducted at atmospheric pressure, compared with the modal mineralogy of the natural Erebus phonolite (from Kelly *et al.*, 2008b)

Experiment or sample number	Experimental conditions					Modal % of phases					
	Dur. (h)	T (°C)	CO <sub>2</sub> /CO	log( <i>f</i> O <sub>2</sub> )	ΔQFM	MG	Anorth	CPX	OL	Ti-mt	F-ap
C_ATM_01	96	950	15	-12.70	-0.92	63.75	30.00	3.75	n.d.	2.50	n.d.
C_ATM_02	96	975	15	-12.30	-0.93	67.55	28.89	0.57	n.d.	2.99	n.d.
C_ATM_03	96	925	15	-13.20	-0.99	32.45	63.59	1.72	n.d.	2.24	n.d.
C_ATM_04	90	1000	15	-11.80	-0.82	78.08	21.56	0.00	n.d.	0.36	n.d.
C_ATM_05	94	1018	15	-11.45	-0.74	97.53	n.d.	n.d.	n.d.	1.27	1.12
C_ATM_06	95	1025	15	-11.30	-0.70	98.12	n.d.	n.d.	n.d.	0.45	1.43
C_ATM_07	94	905	15	-13.60	-1.03	12.57	78.19	5.70	n.d.	3.54	0.00
97018*						65.50	30.60	0.40	1.30	1.70	0.60

MG, matrix glass; OL, olivine; CPX, clinopyroxene; Anorth, anorthoclase; Ti-mt, titanomagnetite; F-ap, fluorapatite; n.d., not detected.

The calculated modal mineralogy of the natural phonolite from Kelly *et al.* (2008b).

#### High-pressure phase equilibria and phase proportions

Table 3 summarizes the modal proportion of phases and associated water content for all runs conducted at pressures from 20 to 300 MPa, at or near QFM. The phase relationships are also presented in isobaric and isothermal diagrams (Figs 3 and 4) displaying either the composition of the coexisting fluid phase (Fig. 3) or the amount of water dissolved in the quenched melt (Fig. 4).

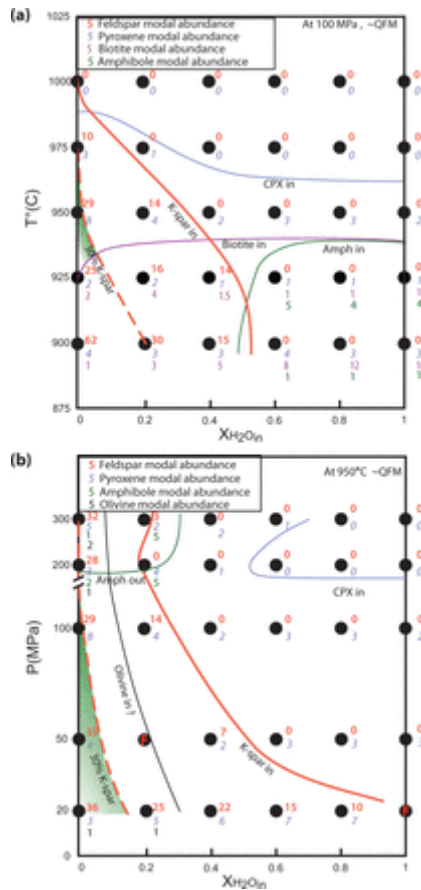


Fig. 3 : (a). Isobaric–polythermal phase relationships of Erebus phonolite at 100 MPa and  $\log(fO_2)$  near QFM. Filled black circles represent the  $T$ – $X_{H_2Ofluid}$  conditions of single experimental charges. Phases lie inside their stability field and the proportion of each major phase is given for each experiment. The red dashed line marks 30% modal proportion of anorthoclase crystals in the run products. The shaded area shows the estimated stability conditions of temperature and  $X_{H_2Ofluid}$  (the mole fraction of  $H_2O$  in the fluid phase), as inferred from the phenocryst assemblage of the Erebus phonolite. The natural modal phase proportion is 65.5% matrix glass, 30.6% anorthoclase feldspar, 1.7% titanomagnetite, 1.3% olivine, 0.4% clinopyroxene and 0.6% fluorapatite (Kelly *et al.*, 2008b). (b) Isothermal–polybaric phase relationships of Erebus phonolite at 950°C and  $\log(fO_2)$  near QFM. (Note the break in the pressure axis.) The red dashed line marks 30% modal proportion of anorthoclase crystals in the run products. The shaded area shows the estimated stability conditions of  $P$ – $X_{H_2Ofluid}$  as inferred from the phenocryst assemblage of the Erebus phonolite. K-spar, potassium feldspar; Amph, amphibole; CPX, clinopyroxene. Runs denoted with ‘F’ in the filled black circles represent experiments in which some volatiles were lost.

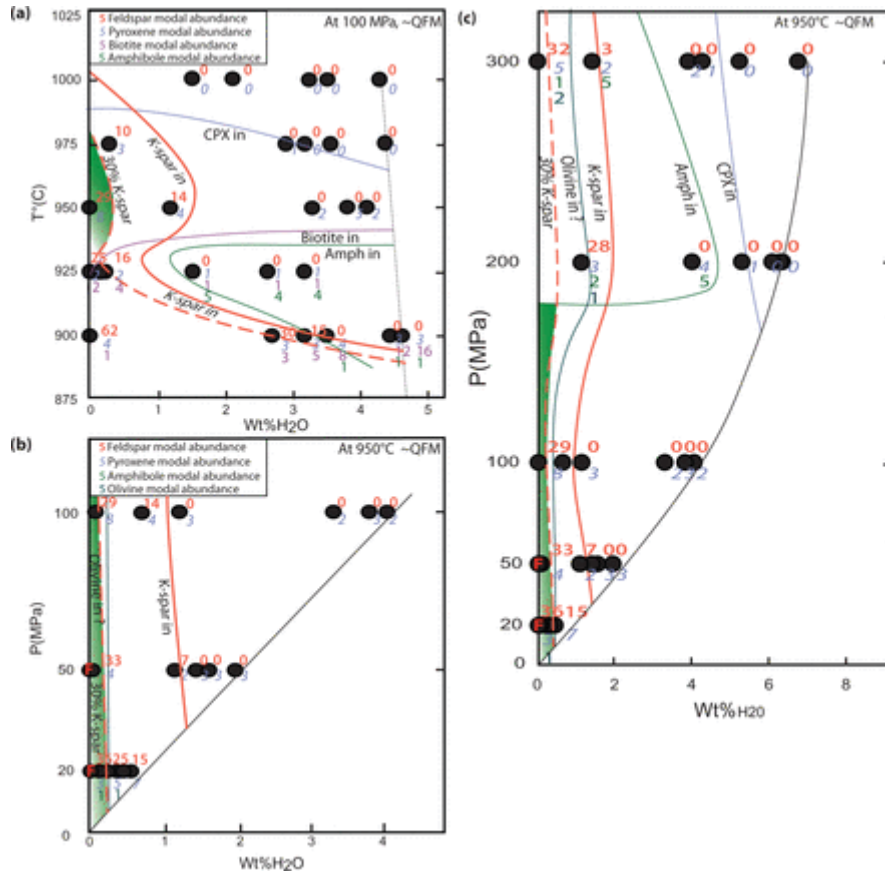


Fig. 4 : (a) Isobaric–polythermal phase relationships of Erebus phonolite at 100 MPa and  $\log(fO_2)$  near QFM. Filled black circles represent the  $T$ –wt %  $H_2O_{\text{fluid}}$  location of single experimental charges. Phases lie inside their stability field and the proportion of each major phase is given for each experiment. The dashed red line denotes 30% modal proportion of anorthoclase crystals in the run products. The shaded area shows the estimated stability conditions of temperature and wt %  $H_2O_{\text{fluid}}$ , as inferred from the phenocryst assemblage of the Erebus phonolite. The natural modal phase proportion is 65.5% matrix glass, 30.6% anorthoclase feldspar, 1.7% titanomagnetite, 1.3% olivine, 0.4% clinopyroxene and 0.6% fluorapatite (Kelly *et al.*, 2008b). The dotted line represents the solubility of water in phonolites from the Montaña Blanca pumice and Laacher See tephra as a function of temperature at 100 MPa as determined by Schmidt & Behrens (2008). (b) Isothermal–polybaric phase relationships of Erebus phonolite at 950°C and  $\log(fO_2)$  near QFM for pressure up to 100 MPa. The red dashed line marks the 30% modal proportion of anorthoclase crystals in the run products. The shaded area shows the estimated stability conditions of  $P$ –wt %  $H_2O_{\text{fluid}}$  as inferred from the phenocryst assemblage of the Erebus phonolite. The black line shows the solubility of water in Erebus phonolitic melt as determined from our experimental charges. (See Fig. 2 for abbreviations.) (c) Same as (b) but for pressure up to 300 MPa.

Table 3 : Experimental conditions, calculated water contents and modal mineralogy of all experiments conducted in high-temperature pressure vessels

Experiment or sample number	Experimental conditions					Recalculated conditions				Modal % of phases						
	Time (h)	T (°C)	P (MPa)	fH <sub>2</sub>	X <sub>H<sub>2</sub>O</sub>	wt % H <sub>2</sub> O*	log(fO <sub>2</sub> ) <sup>†</sup>	ΔQF M	MG	Anort h	CP X	Bio	Am p	Ti- mt	OL	F- ap
<i>AUTEXP01</i>																
97018_AUT_01	117	1000	101	6.92	1.0	4.25 <sup>‡</sup>	-10.30	0.59	100.00	n.d.	n.d.	n.d.	n.d.	n.d.	n.d.	n.d.
97018_AUT_02	117	1000	101	6.92	0.8	3.52*	-10.49	0.40	100.00	n.d.	n.d.	n.d.	n.d.	n.d.	n.d.	n.d.
97018_AUT_03	117	1000	101	6.92	0.6	4.25	-10.74	0.15	100.00	n.d.	n.d.	n.d.	n.d.	n.d.	n.d.	n.d.
97018_AUT_04	117	1000	101	6.92	0.4	3.32*	-11.09	-0.20	100.00	n.d.	n.d.	n.d.	n.d.	n.d.	n.d.	n.d.
97018_AUT_05	117	1000	101	6.92	0.2	2.15	-11.69	-0.80	100.00	n.d.	n.d.	n.d.	n.d.	n.d.	n.d.	n.d.
97018_AUT_11	117	1000	101	6.92	0.0	1.47	-12.30	-1.41	100.00	n.d.	n.d.	n.d.	n.d.	n.d.	n.d.	n.d.
<i>AUTEXP02</i>																
97018_AUT_13	111	1000	51	3.23	1.0	2.76	-10.20	0.69	100.00	n.d.	n.d.	n.d.	n.d.	n.d.	n.d.	n.d.
97018_AUT_14	111	1000	51	3.23	0.8	2.68*	-10.40	0.49	100.00	n.d.	n.d.	n.d.	n.d.	n.d.	n.d.	n.d.
97018_AUT_15	111	1000	51	3.23	0.6	1.59*	-10.65	0.24	100.00	n.d.	n.d.	n.d.	n.d.	n.d.	n.d.	n.d.
97018_AUT_16	111	1000	51	3.23	0.4	1.05*	-11.00	-0.11	100.00	n.d.	n.d.	n.d.	n.d.	n.d.	n.d.	n.d.
97018_AUT_17	111	1000	51	3.23	0.2	1.87*	-11.60	-0.71	100.00	n.d.	n.d.	n.d.	n.d.	n.d.	n.d.	n.d.
97018_AUT_18	111	1000	51	3.23	0.0	1.3*	-12.20	-1.31	100.00	n.d.	n.d.	n.d.	n.d.	n.d.	n.d.	n.d.
<i>AUTEXP03</i>																
97018_AUT_06	118	900	115	10.89	1.0	4.59 <sup>‡</sup>	-12.49	0.07	79.03	n.d.	2.85	15.90	0.55	1.65	n.d.	n.d.
97018_AUT_07	118	900	115	10.89	0.8	4.48 <sup>‡</sup>	-12.69	-0.12	83.33	n.d.	3.10	12.01	0.80	0.77	n.d.	n.d.
97018_AUT_08	118	900	115	10.89	0.6	3.48	-12.94	-0.37	85.62	n.d.	3.90	7.90	0.90	1.69	n.d.	n.d.
97018_AUT_09	118	900	115	10.89	0.4	3.15	-13.29	-0.73	76.27	14.93	3.06	5.30	0.00	0.44	n.d.	n.d.
97018_AUT_10	118	900	115	10.89	0.2	2.66	-13.89	-1.33	62.78	30.26	3.40	3.07	n.d.	0.48	n.d.	n.d.
97018_AUT_12	118	900	115	10.89	0.0	0.00	-14.49	-1.93	31.85	61.97	4.06	1.13	n.d.	1.00	n.d.	n.d.
<i>AUTEXP04</i>																
97018_AUT_25	115	950	102	14.15	1.0	4.05	-11.78	-0.09	97.33	n.d.	2.40	n.d.	n.d.	0.27	n.d.	n.d.
97018_AUT_26	115	950	102	14.15	0.8	3.78	-11.98	-0.28	97.02	n.d.	2.79	n.d.	n.d.	0.19	n.d.	n.d.

Experiment or sample number	Experimental conditions					Recalculated conditions				Modal % of phases						
	Time (h)	T (°C)	P (MPa)	fH <sub>2</sub>	X <sub>H<sub>2</sub>O</sub>	wt % H <sub>2</sub> O*	log(fO <sub>2</sub> ) <sup>‡</sup>	ΔQF M	MG	Anorth h	CP X	Bio	Am p	Ti- mt	OL	F- ap
97018_AUT_27	115	950	102	14.1 5	0.6	unrealistic	-12.23	-0.53	96.90	n.d.	3.5 1	n.d.	n.d.	0.4 0	n.d.	n.d.
97018_AUT_28	115	950	102	14.1 5	0.4	3.28	-12.58	-0.89	97.90	n.d.	2.0 0	n.d.	n.d.	0.1 0	n.d.	n.d.
97018_AUT_29	115	950	102	14.1 5	0.2	1.17	-13.18	-1.49	81.50	14.40	4.0 0	n.d.	n.d.	0.1 3	n.d.	n.d.
97018_AUT_30	115	950	102	14.1 5	0.0	0.00	-13.78	-2.09	63.31	28.76	7.8 0	n.d.	n.d.	0.1 0	n.d.	n.d.
<i>AUTEXP05</i>																
97018_AUT_31	146	975	100	12.1 7	1.0	4.40 <sup>‡</sup>	-11.21	0.07	100.0 0	n.d.	n.d.	n.d.	n.d.	n.d.	n.d.	n.d.
97018_AUT_32	146	975	100	12.1 7	0.8	3.50 <sup>‡</sup>	-11.41	-0.12	100.0 0	n.d.	n.d.	n.d.	n.d.	n.d.	n.d.	n.d.
97018_AUT_33	146	975	100	12.1 7	0.6	3.13	-11.65	-0.37	100.0 0	n.d.	n.d.	n.d.	n.d.	n.d.	n.d.	n.d.
97018_AUT_34	146	975	100	12.1 7	0.4	unrealistic	-12.01	-0.72	100.0 0	n.d.	n.d.	n.d.	n.d.	n.d.	n.d.	n.d.
97018_AUT_35	146	975	100	12.1 7	0.2	2.88	-12.61	-1.33	98.97	n.d.	0.9 5	n.d.	n.d.	0.0 8	n.d.	n.d.
97018_AUT_36	146	975	100	12.1 7	0.0	0.26	-13.21	-1.93	86.64	10.56	2.7 6	n.d.	n.d.	0.0 4	n.d.	n.d.
<i>AUTEXP06</i>																
97018_AUT_37	91	925	100	3.76	1.0	3.16	-11.09	1.03	93.52	n.d.	0.4 9	1.13	4.05	0.8 1	n.d.	n.d.
97018_AUT_38	91	925	100	3.76	0.8	2.62	-11.29	0.83	95.27	n.d.	0.1 7	0.26	3.84	0.4 7	n.d.	n.d.
97018_AUT_39	91	925	100	3.76	0.6	1.49	-11.54	0.58	92.60	n.d.	0.7 9	1.19	4.95	0.4 7	n.d.	n.d.
97018_AUT_40	91	925	100	3.76	0.4	0.00	-11.89	0.23	82.71	14.69	1.0 0	1.50	0.00	0.1 0	n.d.	n.d.
97018_AUT_41	91	925	100	3.76	0.2	0.08	-12.49	-0.37	76.81	16.21	2.3 4	4.35	0.00	0.2 9	n.d.	n.d.
97018_AUT_42	91	925	100	3.76	0.0	0.00	-13.09	-0.97	70.11	25.00	2.2 3	2.16	0.00	0.4 6	n.d.	n.d.
<i>AUTEXP07</i>																
97018_AUT_19	189	950	20	0.45	1.0	0.00	-10.11	1.58	Failed							
97018_AUT_20	189	950	20	0.45	0.8	0.23	-10.31	1.38	82.80	10.00	6.9 0	n.d.	n.d.	0.3 0	n.d.	n.d.
97018_AUT_21	189	950	20	0.45	0.6	0.34	-10.56	1.13	77.00	15.00	7.2 0	n.d.	n.d.	0.8 0	n.d.	n.d.
97018_AUT_22	189	950	20	0.45	0.4	0.48	-10.91	0.78	71.20	21.85	6.4 9	n.d.	n.d.	0.4 7	n.d.	n.d.
97018_AUT_23	189	950	20	0.45	0.2	0.00	-11.51	0.18	69.15	25.30	5.2 0	n.d.	n.d.	0.3 5	<0.5	n.d.
97018_AUT_24	189	950	20	0.45	0.0	0.12	-12.11	-0.42	60.04	36.02	3.4 0	n.d.	n.d.	0.5 4	<0.5	n.d.

Experiment or sample number	Experimental conditions						Recalculated conditions				Modal % of phases					
	Time (h)	T (°C)	P (MPa)	fH <sub>2</sub>	X <sub>H<sub>2</sub>O</sub>	wt % H <sub>2</sub> O*	log(fO <sub>2</sub> ) <sup>‡</sup>	ΔQF M	MG	Anorth h	CP X	Bio	Am p	Timt	OL	F- ap
<i>AUTEXP08</i>																
97018_AUT_43	115	950	50	5.02	1.0	1.96	-11.47	0.22	96.31	n.d.	3.20	n.d.	n.d.	0.50	n.d.	n.d.
97018_AUT_44	115	950	50	5.02	0.8	1.58	-11.66	0.03	96.31	n.d.	3.09	n.d.	n.d.	0.61	n.d.	n.d.
97018_AUT_45	115	950	50	5.02	0.6	1.09	-11.91	-0.22	96.47	n.d.	3.02	n.d.	n.d.	0.50	n.d.	n.d.
97018_AUT_46	115	950	50	5.02	0.4	1.40	-12.27	-0.57	89.92	7.28	2.37	n.d.	n.d.	0.44	n.d.	n.d.
97018_AUT_47	115	950	50	5.02	0.2	0.00	-12.87	-1.18	Failed							
97018_AUT_48	115	950	50	5.02	0.0	0.00	-13.47	-1.78	60.94	33.11	4.12	n.d.	n.d.	1.83	n.d.	n.d.
<i>AUTEXP09</i>																
97018_AUT_49	168	950	300	33.33	1.0	6.69	-11.57	0.13	99.30	n.d.	n.d.	n.d.	n.d.	0.10	n.d.	0.70
97018_AUT_50	168	950	300	33.33	0.8	5.19	-11.76	-0.07	99.80	n.d.	n.d.	n.d.	n.d.	0.05	n.d.	0.15
97018_AUT_51	168	950	300	33.33	0.6	4.24	-12.01	-0.32	98.70	n.d.	1.00	n.d.	n.d.	0.05	n.d.	0.25
97018_AUT_52	168	950	300	33.33	0.4	3.88	-12.36	-0.67	98.99	n.d.	0.95	n.d.	n.d.	0.01	n.d.	0.04
97018_AUT_53	168	950	300	33.33	0.2	1.44	-12.96	-1.27	89.77	2.86	2.48	n.d.	4.76	0.14	n.d.	0.00
97018_AUT_54	168	950	300	33.33	0.0	0.00	-13.57	-1.87	59.68	32.67	4.98	n.d.	0.81	0.23	1.63	0.00
<i>AUTEXP10</i>																
97018_AUT_55	139	950	200		1.0	6.30 <sup>‡</sup>			98.00	n.d.	n.d.	n.d.	n.d.	1.50	n.d.	0.50
97018_AUT_56	139	950	200		0.8	5.98 <sup>‡</sup>			98.00	n.d.	n.d.	n.d.	n.d.	1.50	n.d.	0.50
97018_AUT_57	139	950	200		0.6	6.28 <sup>‡</sup>			98.50	n.d.	n.d.	n.d.	n.d.	1.00	n.d.	0.50
97018_AUT_58	139	950	200		0.4	5.21 <sup>‡</sup>			98.95	n.d.	n.d.	n.d.	n.d.	1.00	n.d.	0.05
97018_AUT_59	139	950	200		0.2	3.94 <sup>‡</sup>			91.61	n.d.	3.57	n.d.	4.76	0.06	n.d.	0.00
97018_AUT_60	139	950	200		0.0	1.06 <sup>‡</sup>			65.62	28.27	3.03	n.d.	1.89	0.05	1.04	0.00
<i>AUTEXP11</i>																
97018_AUT_61	139	950	100	0.06	1.0	4.46 <sup>‡</sup>	-6.19	4.70	96.77	n.d.	1.08	n.d.	n.d.	2.15	n.d.	n.d.
97018_AUT_62	139	950	100	0.06	0.8	4.82 <sup>‡</sup>	-6.38	4.51	93.51	n.d.	2.60	n.d.	n.d.	3.90	n.d.	n.d.
97018_AUT_63	139	950	100	0.06	0.6	4.07 <sup>‡</sup>	-6.63	4.26	95.70	n.d.	2.15	n.d.	n.d.	2.15	n.d.	n.d.
97018_AUT_64	139	950	100	0.06	0.4	3.2 <sup>‡</sup>	-6.98	3.91	93.68	n.d.	4.2	n.d.	n.d.	2.1	n.d.	n.d.

Experiment or sample number	Experimental conditions					Recalculated conditions				Modal % of phases						
	Time (h)	T (°C)	P (MPa)	fH <sub>2</sub>	X <sub>H<sub>2</sub>O</sub>	wt % H <sub>2</sub> O*	log(fO <sub>2</sub> ) <sup>†</sup>	ΔQF M	MG	Anorth h	CP X	Bio	Am p	Ti- mt	OL	F- ap
64											1			1		
97018_AUT- 65	139	950	100	0.06	0.2	1.52 <sup>‡</sup>	-7.58	3.31	85.18	13.63	1.1 4	n.d.	4.54	0.0 6	n.d.	n.d.
97018_AUT- 66	139	950	100	0.06	0.0	0.08 <sup>‡</sup>	-8.19	2.70	73.19	22.52	4.2 2	n.d.	7.04	0.0 7	n.d.	n.d.

MG, matrix glass; Anorth, anorthoclase; CPX, clinopyroxene; Bio, biotite; Amph, amphibole; OL, olivine; Ti-mt, titanomagnetite; F-ap, fluorapatite; n.d., not detected.

\*Wt % H<sub>2</sub>O as determined by FTIR absorption spectroscopy on supra-liquidus charges (AUTEXP01 and 02) and by the by-difference calculation method for crystallized charges.

†Log(fO<sub>2</sub>) at water saturation determined from CoPd sensors following the procedure of Taylor *et al.* (1992). log(fO<sub>2</sub>) in single capsules recalculated based on X<sub>H<sub>2</sub>O</sub> initial except for the case X<sub>H<sub>2</sub>O</sub> = 0 for which an X<sub>H<sub>2</sub>O</sub> = 0.1 value, more representative of the true initial amount of water, has been used.

‡Recalculated values for charges where wt % H<sub>2</sub>O as determined by the by-difference method yields an overestimate (above the H<sub>2</sub>O solubility curve). The wt % H<sub>2</sub>O are recalculated based on the most hydrous charge wt % H<sub>2</sub>O being equal to that predicted by the solubility curve.

At 100 MPa and water-rich conditions, the liquidus is located between 975 and 950°C and is marked by the co-precipitation of clinopyroxene and titanomagnetite, both phases sharing the same liquidus curve. At low water contents (<3 wt %), anorthoclase joins the stable assemblage between 975 and 1000°C. Between 925 and 950°C, and irrespective of water content, biotite crystallizes, displaying an essentially flat in-curve in the T-X<sub>H<sub>2</sub>O</sub> section. Amphibole appears within a similar temperature interval but is restricted to high water contents (>2 wt %), crystallizing in all charges free of anorthoclase, suggesting limited overlap between the respective stability fields of these phases. Precipitation of amphibole in Erebus phonolites at 100 MPa would imply both temperatures lower than 950°C and melt water contents higher than 2 wt % (Fig. 4a). In contrast to the proportions of clinopyroxene and titanomagnetite, which vary little over the T-X<sub>H<sub>2</sub>O</sub> space explored, the proportion of biotite increases with decreasing temperature and increasing water content, whereas that of feldspar increases with lower water content and lower temperature (Fig. 3). The natural modal abundance of feldspar (i.e. of the starting rock) is reproduced at a temperature close to 950°C and at water contents below 1 wt %. Hence, a temperature of 950°C was used in the second series of polybaric experiments (Fig. 3b).

At pressures above 200 MPa amphibole is present at 950°C, showing that increasing pressure expands the thermal stability of amphibole in Na-phonolite magmas (Fig. 4c). Feldspar is stable throughout the range of pressures explored at low water contents. In the P-X<sub>H<sub>2</sub>O</sub> projection (Fig. 4b and c), the anorthoclase liquidus curve has a vertical slope, although small inflections occur between 150 and 200 MPa. It is unclear whether this is real or results from

error in water content determination. The natural proportion of feldspar is re-created in the pressure range 20 to <200 MPa and water contents below 1 wt % (Fig. 4b and c). However, at pressures of 200 MPa and above, crystallization of 30 wt % anorthoclase in Erebus phonolite necessarily occurs in the presence of amphibole (Fig. 4c). Fluorapatite was detected at a pressure of 200 MPa and high water contents. Olivine is observed in experimental charges at pressures of 20, 200 and 300 MPa and low water contents (<2 wt %). The non-detection of olivine in charges at 50 and 100 MPa is probably due to its low modal abundance (<1% in run products) making it easy to overlook.

Six experimental charges at 950°C, 100 MPa and over a range of  $X_{H_2O}$  were produced under highly oxidizing conditions (NNO + 4) to assess the effect of  $fO_2$  on phase stabilities (97018\_AUT\_61 to 66). It should be noted that, owing to the decrease in  $fH_2O$  (resulting from the increase in  $CO_2$ ) at constant  $fH_2$ , the  $fO_2$  reached in the driest charges of the oxidized run is around NNO + 2 (Table 3). As shown in Fig. 5, the main difference compared with QFM conditions is that amphibole is stable together with feldspar at low water contents; that is, unlike the natural assemblage (Fig. 5). The decrease in feldspar abundance (and to a lesser extent of clinopyroxene, Table 3) in the oxidized charges relative to those at QFM (Fig. 5) suggests that amphibole crystallization proceeds at the expense of anorthoclase (and clinopyroxene), consistent with the limited overlap of the respective stability fields noted above. That an increase in  $fO_2$  increases the thermal stability of Ca-amphibole has also been documented in metaluminous granite (Dall'Agnol *et al.*, 1999).

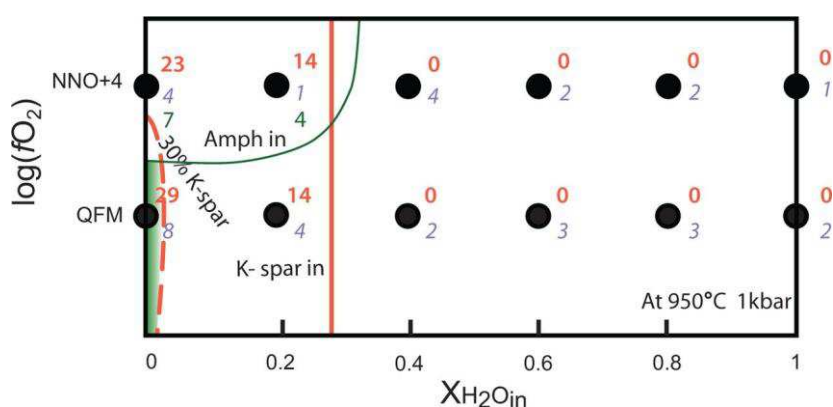


Fig. 5 : Phase relationship with varying  $\log(fO_2)$  and  $X_{H_2Oin}$  of Erebus phonolite at 100 MPa and 950°C. Filled black circles represent the  $\log(fO_2)$ – $X_{H_2Oin}$  location of single experimental charges. Phases lie inside their stability field and the proportion of each major phase is given for each experiment. The red dashed line marks 30% modal proportion of anorthoclase crystals in the run products. The shaded area shows the estimated stability conditions of T–wt %  $H_2O_{fluid}$  as inferred from the phenocryst assemblage of the Erebus phonolite. (See Figs 1 and 2 for abbreviations.)

### Phase compositions

The small size of biotite, titanomagnetite and most of the clinopyroxene prevented the acquisition of good electron microprobe analyses. In some charges, however, clinopyroxene grains were large enough to be analysed and their composition is reported in Table 4 (low totals reflect the electron probe conditions: 2 nA, 10 kV and incomplete mobilization of Si). The natural clinopyroxene composition ( $W_{O46}E_{N37}F_{S16}$ ) is most closely reproduced at 950°C and 20 MPa (Table 4, Fig. 6). Although no clinopyroxene from charges lying within the

stability domain inferred for the natural assemblage could be analysed, clinopyroxene in AUT23, which is very close to this stability window, shows very good agreement with the natural counterpart ( $Wo_{49}En_{36}Fs_{16}$ ), and the Fe/Mg partition coefficient with the liquid (Table 4).

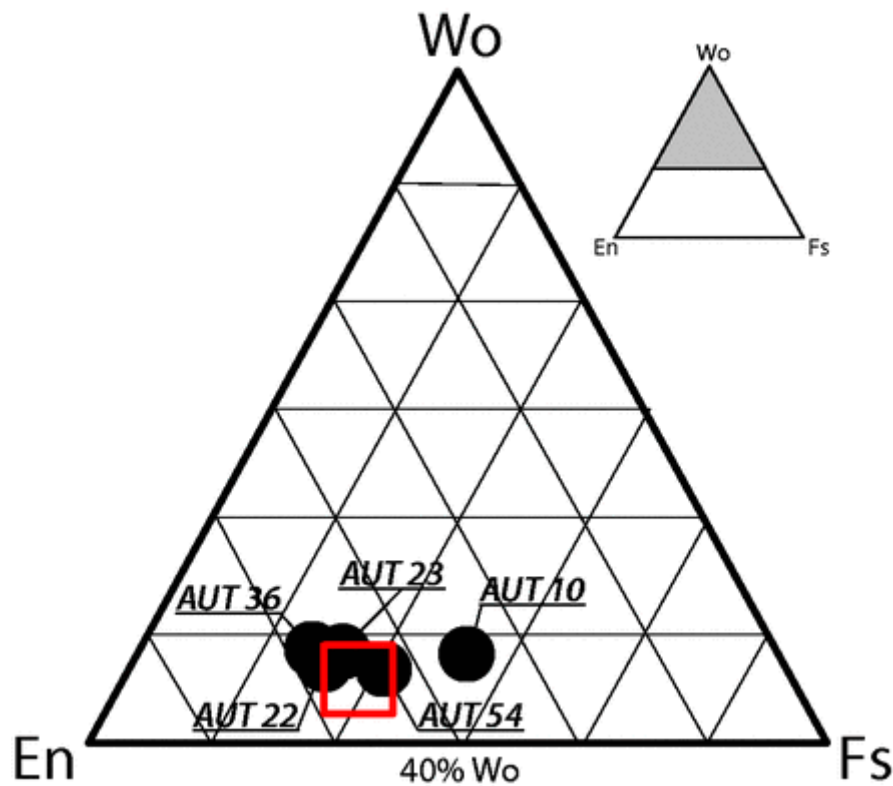


Fig. 6 : Ternary diagram of the chemical composition of pyroxene grains from pressurized experiments reported in Table 4. The end-members in the diagram are wollastonite (Wo;  $Ca_2Si_2O_6$ ), enstatite (En;  $Mg_2Si_2O_6$ ) and ferrosilite (Fs;  $Fe_2SiO_6$ ). The rectangle shows the composition of the natural cpx for reference (Kelly *et al.*, 2008b). It should be noted that the ternary diagram extends only to 40% Wo as shown by the shaded area in the upper right diagram.

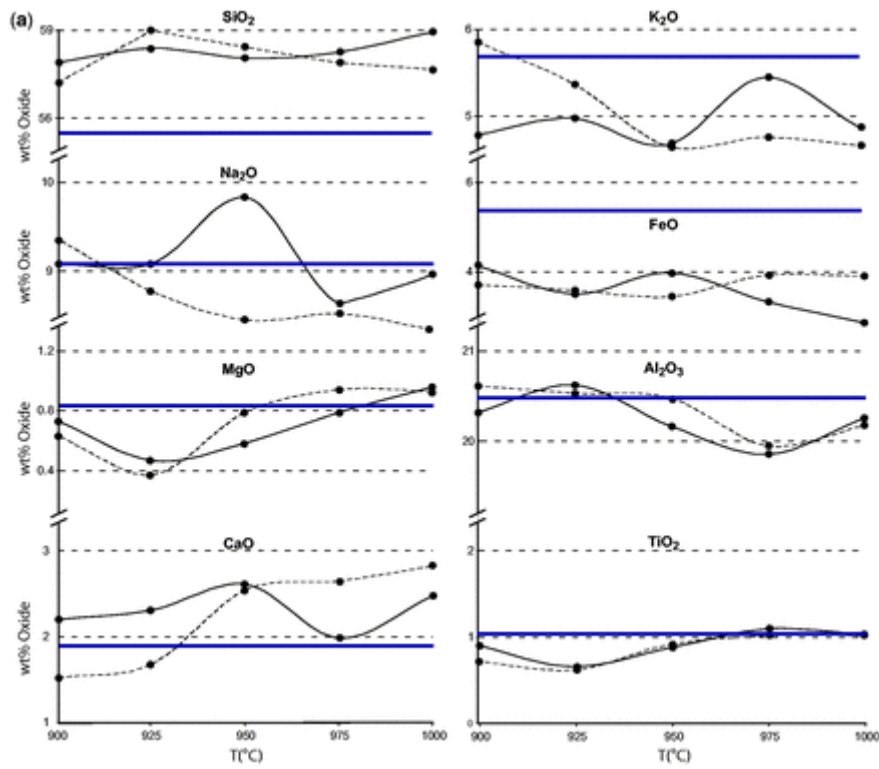


Fig. 7 : Connected scatter plots showing the evolution of the residual glass in term of eight major elements; SiO<sub>2</sub>, Na<sub>2</sub>O, MgO, CaO, K<sub>2</sub>O, FeO, Al<sub>2</sub>O<sub>3</sub>, TiO<sub>2</sub> (from analyses recalculated to 100%) (a) with temperature, at a pressure of 100 MPa and log( $fO_2$ ) near QFM, and (b) with pressure, at a temperature of 950°C and log( $fO_2$ ) near QFM. Continuous lines represent charges at  $X_{H_2O_{in}} = 0$ ; black dashed lines represent charges at  $X_{H_2O_{in}} = 0.2$ . Bold horizontal lines represent the concentration of each element in the natural glass (Eschenbacher, 1998).

Table 4 : Electron microprobe analyses of clinopyroxene from the experimental charges

Experiment:	Natural cpx	AUTEXP03		AUTEXP05		AUTEXP07				AUTEXP09	
		(100 MPa; 900°C)		(100 MPa; 975°C)		(20 MPa; 950°C)				(300 MPa; 950°C)	
	<i>n</i> :	AUT10 ( $X_{H_2O} = 0.2$ )		AUT36 ( $X_{H_2O} = 0$ )		AUT22 ( $X_{H_2O} = 0.4$ )		AUT23 ( $X_{H_2O} = 0.2$ )		AUT54 ( $X_{H_2O} = 0$ )	
	19	3	SD	3	SD	2	SD	2	SD	6	SD
SiO <sub>2</sub>	50.89	48.01	1.02	48.43	1.94	49.00	1.29	48.14	0.41	48.96	1.01
TiO <sub>2</sub>	1.35	1.43	0.38	1.71	0.18	1.51	0.60	1.09	0.16	1.49	0.31
Al <sub>2</sub> O <sub>3</sub>	2.81	5.95	1.90	5.06	2.31	3.04	1.21	2.52	0.34	3.05	0.79
FeO	9.54	12.68	0.65	6.52	0.22	8.01	0.09	8.85	0.28	11.55	1.06
MnO	0.65	0.83	0.27	0.63	0.08	0.80	0.11	0.64	0.02	0.82	0.26
MgO	12.23	7.07	0.87	10.80	1.16	11.65	0.87	11.49	0.17	10.39	0.52
CaO	21.13	18.60	2.22	19.38	1.69	20.45	0.77	21.74	0.36	20.78	1.04
Na <sub>2</sub> O	0.93	1.68	0.30	1.32	0.68	1.00	0.32	0.89	0.01	1.09	0.15
K <sub>2</sub> O		0.50	0.31	0.21	0.14	0.19	0.16	0.19	0.12	0.11	0.07
Total	99.53	96.73	0.58	94.07	2.09	95.64	0.66	95.56	1.12	98.24	0.91
Fe <sub>T</sub> /Mg	0.44	1.01		0.34		0.39		0.43		0.62	
Fe <sub>T</sub> /(Fe <sub>T</sub> + Mg)	0.30	0.50		0.25		0.28		0.30		0.38	
Fe <sub>2</sub> /(Fe <sub>2</sub> + Mg)	0.27	0.50		0.25		0.27		0.21		0.32	
Wo	46.34	48.50		49.07		47.65		48.71		46.95	
En	37.32	25.67		38.03		37.78		35.81		32.68	
Fs	16.33	25.82		12.89		14.57		15.48		20.38	
Fe <sub>T</sub> /Mg in glass	3.62	3.31		2.37		3.78		3.36		4.72	
$K_d$ (Fe/Mg CPX–Melt)	0.12	0.30		0.14		0.10		0.13		0.13	

- The composition of the natural cpx (Kelly *et al.*, 2008b) is given for reference. The Fe/Mg ratio, Fe and Fe<sup>2+</sup> numbers are given together with the partition coefficient ( $K_d$ ) for the Fe/Mg ratio between cpx and liquid. Clinopyroxene endmembers are wollastonite (Wo; Ca<sub>2</sub>Si<sub>2</sub>O<sub>6</sub>), enstatite (En; Mg<sub>2</sub>Si<sub>2</sub>O<sub>6</sub>) and ferrosilite (Fs; Fe<sub>2</sub>SiO<sub>6</sub>).

Fluorapatite composition could not be measured accurately because of the small size of crystals and groundmass contamination; fluorine was nevertheless abundant in all analysed apatite. Amphibole is present mostly as kaersutite or ferropargasite in the cooler experiments. Compositions are reported in Table 5, and are characterized by elevated Ti and K contents. Their Al content does not seem to vary significantly with pressure, contrary to what is found for other intermediate to silicic magmas (e.g. Prouteau & Scaillet, 2003). Olivine compositions in the experimental charges are reported in Table 6 (note that the slightly elevated Al<sub>2</sub>O<sub>3</sub> content in some olivine grains is probably due to contamination of the analysis by surrounding glass) and ranges between Fo<sub>49</sub> and Fo<sub>53</sub> at 20 and 200 MPa [i.e. close to the natural olivine (Fo<sub>50</sub>)], whereas that produced at 300 MPa has a significantly lower Fo content (Fo<sub>39</sub>). Feldspars in the experimental charges are all anorthoclase with Ab contents between

61 and 67%, An contents between 6 and 22%, and Or contents between 33 and 12%. Natural anorthoclase crystals show significant zonation and a detailed comparison with the experimental products will be investigated in a future study. To a first order, however, the bulk composition of the natural anorthoclase is most closely reproduced in high-pressure experiments at 950°C, and in 0.1 MPa experiments at 975°C.

Table 5 : Amphibole compositions (wt %) obtained by electron microprobe analysis (in wt % oxide)

Experiment :  n:	AUTEXP03 (100 MPa; 900°C)						AUTEXP06 (100 MPa; 925°C)						AUTEXP09 (300 MPa; 950°C)		AUTEXP10 (200 MPa; 950°C)	
	AUT06 ( $X_{H_2O} = 1$ )		AUT07 ( $X_{H_2O} = 0.8$ )		AUT08 ( $X_{H_2O} = 0.6$ )		AUT37 ( $X_{H_2O} = 1$ )		AUT38 ( $X_{H_2O} = 0.8$ )		AUT39 ( $X_{H_2O} = 0.6$ )		AUT53 ( $X_{H_2O} = 0.2$ )		AUT59 ( $X_{H_2O} = 0.2$ )	
	5	SD	7	SD	4	SD	7	SD	6	SD	7	SD	7	SD	6	SD
SiO <sub>2</sub>	38.34	0.43	37.62	0.34	38.24	0.49	40.2 2	0.6 2	40.0 3	0.6 2	39.3 6	0.4 9	40.19	0.86	39.80	0.69
TiO <sub>2</sub>	3.79	0.22	3.97	0.34	4.12	0.14	4.09	0.2 6	4.49	0.3 0	4.83	0.3 8	5.69	0.35	5.50	0.20
Al <sub>2</sub> O <sub>3</sub>	11.19	0.54	11.14	0.43	10.67	0.17	11.2 6	0.4 7	11.3 3	0.5 0	11.4 1	0.4 5	11.06	0.29	11.44	0.38
FeO	17.26	0.71	16.56	0.60	16.54	0.40	15.4 6	0.3 3	15.5 7	0.5 3	15.7 0	0.4 3	14.83	0.74	13.28	0.41
MnO	0.63	0.08	0.63	0.17	0.62	0.03	0.50	0.1 6	0.61	0.1 2	0.46	0.1 9	0.52	0.18	0.48	0.05
MgO	8.33	0.10	8.45	0.17	8.72	0.18	10.4 0	0.2 7	10.1 8	0.4 1	9.73	0.1 8	9.84	0.41	10.68	0.31
CaO	10.81	0.37	10.76	0.16	10.89	0.11	11.4 0	0.3 2	11.3 8	0.1 5	11.4 4	0.4 7	10.98	0.28	10.72	0.19
Na <sub>2</sub> O	2.67	0.10	2.64	0.08	2.76	0.04	2.75	0.0 9	2.82	0.0 5	2.71	0.0 8	2.79	0.09	2.78	0.12
K <sub>2</sub> O	1.28	0.09	1.24	0.12	1.16	0.11	1.27	0.1 2	1.29	0.1 3	1.28	0.0 8	1.33	0.09	1.18	0.07
Total	94.29	1.83	93.02	1.32	93.71	1.34	97.3 4	0.9 5	97.6 9	0.7 6	96.9 2	1.2 5	97.22	1.47	95.98	0.64
Name	Potassian titanian ferropargasit e		Potassian titanian ferropargasit e		Titanian ferropargasit e		Kaersutite		Kaersutite		Potassian kaersutite		Potassian kaersutite		Kaersutite	

Table 6 : Electron microprobe analyses of olivine from the experimental charges

	Nat ol <sup>*</sup>		AUTEXP07 (20 MPa; 950°C)		AUTEXP09 (300 MPa; 950°C)		AUTEXP10 (200 MPa; 950°C)	
Experiment:	AUT23 ( $X_{H_2O} = 0.2$ )		AUT24 ( $X_{H_2O} = 0$ )		AUT54 ( $X_{H_2O} = 0$ )		AUT60 ( $X_{H_2O} = 0.2$ )	
<i>n</i> :	67	1	2	SD	6	SD	1	
SiO <sub>2</sub>	34.80	34.21	34.39	0.63	32.62	0.95	33.87	
TiO <sub>2</sub>		0.17	0.09	0.01	0.36	0.62	0.40	
Al <sub>2</sub> O <sub>3</sub>	0.01	0.08	0.60	0.69	0.06	0.05	1.20	
FeO	38.33	35.39	33.61	0.27	44.83	0.71	36.50	
MnO	2.45	3.08	2.60	0.27	2.62	0.17	2.27	
MgO	23.53	23.19	23.05	0.82	17.86	1.09	21.67	
CaO	0.50	0.43	0.48	0.06	0.71	0.28	0.54	
K <sub>2</sub> O		0.00	0.22	0.19	0.05	0.05	0.21	
Total	99.62	96.57	95.34	0.48	99.17	2.14	97.47	
Fo	50.30	51.42	52.71		39.68		49.45	
Fa	45.96	44.02	43.13		55.87		46.72	
Te	2.98	3.88	3.37		3.31		2.94	
Ca-Ol	0.77	0.68	0.78		1.14		0.88	

- \*The composition of the natural olivine (Kelly *et al.*, 2008b) is given for reference. Olivine endmembers are tephroite (Te; Mn<sub>2</sub>SiO<sub>4</sub>), forsterite (Fo; Mg<sub>2</sub>SiO<sub>4</sub>), fayalite (Fa; Fe<sub>2</sub>SiO<sub>4</sub>) and Ca-rich olivine (Ca-Ol).

Table 7 : Electron microprobe analyses of glasses from all the experimental charges

Ex p.:	AUTEXP01 (100 MPa; 1000°C)					AUTEXP02 (50 MPa; 1000°C)					AUTEXP03 (100 MPa; 900°C)					AUTEXP04 (100 MPa; 950°C)								
	AU T01	AU T02	AU T03	AU T04	AU T05	AU T11	AU T13	AU T14	AU T15	AU T16	AU T17	AU T18	AU T06	AU T07	AU T08	AU T09	AU T10	AU T12	AU T25	AU T26	AU T27	AU T28	AU T29	AU T30
n:	10	10	8	9	10	10	8	7	9	7	10	10	5	6	5	5	5	6	7	7	7	7	7	6
Si	56.0	56.4	55.4	56.4	56.7	58.1	57.0	56.9	57.1	57.2	57.7	58.0	57.1	57.1	57.5	56.6	56.0	58.4	56.4	56.5	57.2	56.6	57.7	58.5
O <sub>2</sub>	8	2	2	9	7	4	7	9	0	0	5	2	9	0	6	2	7	1	1	8	8	9	4	2
Ti	0.97	0.96	0.95	1.01	0.99	1.01	0.96	1.04	0.97	0.99	0.97	1.06	0.48	0.62	0.63	0.93	0.70	0.91	0.96	0.94	0.96	0.94	0.90	0.88
O <sub>2</sub>																								
Al <sub>2</sub>	18.9	19.1	18.6	18.9	19.3	19.4	19.1	19.0	19.2	19.4	19.2	19.2	19.8	19.3	19.5	19.1	19.7	19.9	18.7	18.9	19.4	19.0	19.7	19.8
O <sub>3</sub>	8	6	3	9	7	9	6	3	4	3	7	4	3	3	2	0	0	9	1	0	3	4	5	2
Fe	4.16	4.28	4.24	4.07	3.83	2.83	4.33	4.08	4.10	4.13	3.60	3.53	2.98	3.15	3.21	4.22	3.62	4.16	4.27	4.12	4.29	4.08	3.39	4.01
O																								
Mn	0.13	0.19	0.12	0.28	0.28	0.19	0.13	0.27	0.27	0.31	0.19	0.17	0.18	0.39	0.32	0.16	0.26	0.10	0.30	0.20	0.19	0.24	0.22	0.18
O																								
Mg	0.89	0.89	0.85	0.91	0.91	0.95	0.89	0.88	0.90	0.87	0.89	0.91	0.26	0.44	0.36	0.71	0.61	0.73	0.90	0.92	0.91	0.88	0.78	0.59
O																								
Ca	2.59	2.60	2.53	2.76	2.77	2.44	2.57	2.55	2.64	2.60	2.69	2.56	1.94	1.97	2.33	1.86	1.49	2.22	2.62	2.57	2.71	2.43	2.51	2.63
O																								
Na	7.91	8.08	7.63	7.82	8.21	8.28	8.41	8.20	8.01	8.21	8.31	8.50	8.20	8.23	8.36	8.51	9.15	8.78	8.02	8.07	8.04	8.30	8.34	8.70
O <sub>2</sub>																								
K <sub>2</sub>	4.49	4.48	4.40	4.55	4.58	4.80	4.61	4.54	4.53	4.56	4.52	4.89	4.45	4.44	4.53	5.01	5.73	4.82	4.45	4.49	4.54	4.50	4.58	4.70
O																								
P <sub>2</sub>	0.42	0.36	0.37	0.56	0.44	0.35	0.28	0.32	0.36	0.33	0.41	0.48	0.25	0.06	0.43	0.28	0.27	0.40	0.37	0.34	0.40	0.20	0.29	0.37
O <sub>5</sub>																								
F	<dl	<dl	<dl	<dl	<dl	<dl	<dl	0.36	<dl	<dl	<dl	<dl	0.22	0.32	0.18	0.25	0.24	0.26	0.11	0.16	0.35	0.27	0.27	0.31
Cl	0.08	0.09	0.08	0.10	0.09	0.09	0.08	0.08	0.09	0.11	0.09	0.08	0.09	0.11	0.08	0.08	0.14	0.09	0.07	0.08	0.07	0.07	0.08	0.08
Tot al	96.6	97.6	95.3	97.6	98.4	98.6	98.5	98.3	98.3	98.9	99.0	99.6	96.0	96.1	97.5	97.7	98.0	100.0	97.2	97.3	99.1	97.6	98.8	100.0
	6	1	6	3	7	8	3	3	7	5	3	1	9	5	3	2	0	87	0	5	6	4	6	79
Ex p.:	AUTEXP05 (100 MPa; 975°C)					AUTEXP06 (100 MPa; 925°C)					AUTEXP07 (20 MPa; 950°C)					AUTEXP08 (50 MPa; 950°C)								
	AU T31	AU T32	AU T33	AU T34	AU T35	AU T36	AU T37	AU T38	AU T39	AU T40	AU T41	AU T42	AU T19	AU T20	AU T21	AU T22	AU T23	AU T24	AU T43	AU T44	AU T45	AU T46	AU T47	AU T48
n:	7	7	7	6	7	7	7	7	7	7	7	7	7	7	7	7	6	6	7	5	5	5	6	7
Si	55.4	56.4	56.7	55.9	56.6	57.8	57.6	57.8	58.4	58.9	58.6	59.2	56.4	57.3	57.7	57.5	57.1	57.6	56.3	56.7	56.8	56.7	55.5	55.7
O <sub>2</sub>	9	0	6	7	5	8	0	7	7	1	7	2	5	0	8	8	2	8	8	4	0	0	8	5
Ti	0.96	1.01	0.97	0.99	0.99	1.09	0.76	0.63	0.64	0.68	0.61	0.66	0.67	0.63	0.68	0.57	0.63	0.89	0.84	0.87	0.76	0.86	0.97	1.04
O <sub>2</sub>																								
Al <sub>2</sub>	18.6	18.8	19.1	18.7	19.0	19.2	19.2	19.4	20.1	20.0	19.9	20.4	20.2	20.1	19.9	19.9	20.0	20.4	19.0	19.2	19.3	19.5	19.6	19.7
O <sub>3</sub>	6	6	8	0	3	4	7	5	0	2	3	2	1	3	5	9	8	7	7	7	5	8	9	4
Fe	3.76	4.24	4.11	3.85	3.82	3.32	3.97	3.50	3.40	3.39	3.56	3.54	4.59	3.58	3.48	3.43	3.89	2.32	4.12	3.91	3.98	3.83	5.25	4.80
O																								
Mn	0.15	0.15	0.32	0.17	0.20	0.34	0.23	0.30	0.27	0.16	0.09	0.09	0.31	0.25	0.14	0.19	0.26	0.20	0.25	0.24	0.21	0.18	0.20	0.23
O																								
Mg	0.69	0.73	0.77	0.81	0.92	0.79	0.52	0.50	0.43	0.47	0.37	0.47	0.71	0.58	0.62	0.51	0.65	0.53	0.90	0.79	0.75	0.73	0.53	0.63
O																								
Ca	2.96	2.83	2.76	2.70	2.59	1.97	2.08	2.20	2.00	1.85	1.67	2.34	1.02	1.51	1.36	1.16	1.36	1.09	2.38	2.15	2.18	2.07	1.48	1.49
O																								
Na	8.62	7.85	8.13	8.59	8.34	8.76	8.14	8.25	8.18	8.52	8.71	8.87	9.38	8.55	8.46	8.66	8.88	8.94	7.81	8.09	8.24	8.05	9.29	9.80
O <sub>2</sub>																								
K <sub>2</sub>	4.25	4.09	4.28	4.31	4.64	5.41	4.69	4.69	4.74	5.03	5.34	5.04	6.10	5.40	5.43	5.70	5.59	6.02	4.55	4.67	4.78	4.86	6.10	5.92
O																								
P <sub>2</sub>	0.31	0.27	0.27	0.21	0.26	0.28	0.19	0.24	0.16	0.31	0.34	0.43	0.30	0.24	0.15	0.13	0.14	0.13	0.27	0.20	0.32	0.20	0.25	0.30
O <sub>5</sub>																								
F	0.13	0.13	0.08	0.22	0.34	0.23	0.18	0.33	0.20	0.20	0.09	0.24												
Cl	0.09	0.08	0.10	0.09	0.08	0.08	0.07	0.08	0.07	0.08	0.11	0.10												
Tot al	96.0	96.6	97.7	96.6	97.8	99.3	97.7	98.0	98.6	99.6	99.4	101.0	99.7	98.1	98.0	97.9	98.5	98.2	96.5	96.9	97.3	97.0	99.3	99.7
	9	4	3	0	7	8	1	2	7	1	9	43	4	6	6	4	9	7	6	2	7	8	4	0

Ex p.:	AUTEXP09						AUTEXP10						AUTEXP11						C_ATM (0.1 MPa)						Natural glasses <sup>1</sup>
	(300 MPa; 950°C)						(200 MPa; 950°C)						(100 MPa; 950°C; oxidized)						(950 °C)	(975 °C)	(925 °C)	(100 °C)	(101 °C)	(102 °C)	
	AU T49	AU T50	AU T51	AU T52	AU T53	AU T54	AU T55	AU T56	AU T57	AU T58	AU T59	AU T60	AU T61	AU T62	AU T63	AU T64	AU T65	AU T66	01	02	03	04	05	06	
n:	7	7	7	7	7	6	10	10	9	7	7	10	7	7	7	7	7	7	10	10	10	10	7	4	18
Si	53	55	54	56	57	56	52	53	53	53	53	54	53	53	53	54	55	54	55.6	55.5	55.4	55.6	55.9	56.6	55.1
O <sub>2</sub>	71	02	81	00	05	84	86	17	00	19	79	08	16	87	95	76	56	01	2	6	4	9	0	8	1
Ti	0.9	0.9	0.9	0.9	0.8	0.6	0.8	0.9	0.9	0.8	0.8	0.8	0.8	0.8	0.8	0.8	0.7	0.8	0.96	0.96	0.96	1.15	0.95	0.82	1.03
O <sub>2</sub>	1	3	4	3	0	4	9	0	4	8	1	7	3	5	0	3	4	4							
Al <sub>2</sub> O <sub>3</sub>	18	19	19	19	19	20	18	18	18	18	18	19	18	18	18	19	19	19	19.4	19.2	19.3	18.9	19.7	19.9	19.8
O <sub>3</sub>	49	05	01	34	74	13	17	35	18	79	02	01	58	68	66	11	43	31	6	0	7	2	6	7	5
Fe	3.8	3.7	4.0	3.1	3.2	4.0	4.3	4.1	4.0	4.2	3.9	4.2	3.1	2.6	2.6	2.5	2.4	3.7	4.87	5.40	5.09	5.57	4.53	3.72	5.34
O	5	5	8	9	4	4	3	7	0	9	2	7	8	1	9	8	2	1							
M	0.2	0.2	0.2	0.1	0.2	0.1	0.1	0.1	0.2	0.2	0.2	0.2	0.1	0.1	0.1	0.1	0.2	0.2	0.27	0.30	0.39	0.23	0.22	0.23	0.27
nO	0	1	0	6	4	9	9	8	1	3	2	6	7	0	8	1	0	3							
MgO	0.8	0.8	0.8	0.8	0.6	0.5	0.8	0.8	0.8	0.7	0.7	0.8	0.7	0.7	0.7	0.7	0.5	0.7	0.82	0.87	0.93	0.98	0.86	0.68	0.83
O	4	6	6	1	0	1	1	3	7	8	4	0	8	4	1	6	4	4							
Ca	2.3	2.4	2.3	2.4	1.9	1.8	2.4	2.3	2.5	2.3	2.3	2.0	2.5	2.3	2.4	2.4	1.7	1.7	1.13	1.95	1.31	2.12	1.06	0.58	1.88
O	7	0	6	7	1	6	0	8	3	4	0	9	2	2	9	2	8	4							
Na <sub>2</sub> O	7.1	6.8	7.4	7.2	8.0	8.8	7.3	7.6	7.7	8.1	8.2	8.7	7.7	7.7	7.8	8.1	8.6	9.0	8.97	8.56	9.38	8.32	8.30	8.17	9.07
O	4	9	7	0	7	4	2	4	2	6	7	2	4	4	7	1	2	3							
K <sub>2</sub> O	4.3	4.0	4.4	4.3	5.0	5.3	4.4	4.4	4.3	4.2	4.5	5.2	4.4	4.4	4.4	4.5	5.0	5.5	6.46	6.00	6.25	5.34	7.11	6.32	5.65
O	4	8	7	8	9	4	6	5	7	4	3	9	4	1	0	5	6	2							
P <sub>2</sub> O <sub>5</sub>	0.3	0.3	0.2	0.2	0.3	0.2	0.2	0.3	0.3	0.2	0.3	0.3	0.3	0.1	0.2	0.2	0.1	0.3	0.33	0.48	0.38	0.46	0.28	0.26	0.3
O	1	7	4	8	1	8	9	2	7	0	2	6	0	2	4	6	8	0							
F							0.0	0.1	0.0	0.1	0.0	0.0	0.1	0.2	0.1	0.1	0.1	0.1					0.06	<dl	
							6	3	6	5	9	9	2	0	6	3	2	2							
Cl							0.0	0.0	0.0	0.0	0.0	0.1	0.0	0.0	0.0	0.0	0.0	0.1					0.04	0.00	
							8	8	9	9	8	2	9	7	8	7	9	3							
Total	92.17	93.56	94.45	94.78	97.04	98.68	91.93	92.64	92.40	93.38	94.19	96.00	92.03	91.80	92.28	93.77	94.84	95.75	98.90	99.28	99.49	98.78	99.19	97.55	99.33

\*Natural sample glass composition from Eschenbacher (1998). <dl, below detection limit. No glass analyses from experiment C\_ATM 07 could be obtained owing to its high crystallinity level.

Analyses of glasses are reported in Table 7 and Fig. 7. Figure 7a shows the variation in glass composition for charges at  $X_{H_2O_{in}} = 0$  and  $X_{H_2O_{in}} = 0.2$  with respect to temperature at a constant pressure of 100 MPa. Although the anorthoclase composition is fairly similar to the bulk-rock composition, its crystallization lowers the SiO<sub>2</sub> and CaO contents of the residual melt while increasing that of K<sub>2</sub>O and keeping Na<sub>2</sub>O constant. The crystallization of clinopyroxene decreases MgO and results in a slight increase in Al<sub>2</sub>O<sub>3</sub> with decreasing temperature. Glasses produced at high  $fO_2$  are similar to those produced at QFM, except for a significantly lower FeO<sub>tot</sub> content (Table 7), owing in particular to a higher modal proportion of magnetite (Table 3). This also results in a lower Fe/Mg ratio of melts produced at high  $fO_2$  (in the range 3.5–4.5 vs 4.5–6.5 at QFM).

Figure 7b shows the residual glass composition of reduced charges at  $X_{H_2O_{in}} = 0$  and  $X_{H_2O_{in}} = 0.2$  with respect to pressure at a constant temperature of 950°C. Although most charges (at a given  $X_{H_2O}$ ) contain comparable modal abundance of minerals, the amount of anorthoclase does increase with decreasing pressure, causing an increase in K<sub>2</sub>O and a decrease in CaO content in the residual glass. The slight increase in Na<sub>2</sub>O with decreasing pressure is linked to the less albite-rich composition of the anorthoclase, which tends to be stable at lower pressure (to be discussed in a future study). Other major elements vary little (or in a non-systematic way) with decreasing pressure.

In Fig. 7a and b, the composition of the natural glass is also plotted as a bold horizontal line. The natural glass composition is most closely reproduced at 950°C and pressures between 50 and 20 MPa, although the agreement is far from perfect and some oxide contents can be reproduced under different conditions. At atmospheric pressure, experimental charges produced between 925 and 1000°C are all close to the natural glass composition. The closest match is found at 975°C.

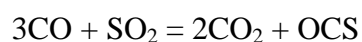
## Discussion

### Constraints on the shallow plumbing system of Erebus

Isobaric phase-equilibrium experiments at 0.1 and 100 MPa, spanning a temperature range from 900 to 1025°C, reproduce the natural Erebus phonolite phase proportions and compositions at a temperature of  $950 \pm 25^\circ\text{C}$ . In addition, our phase-equilibrium data (Fig. 3) set a robust lower temperature limit of 925°C for the Erebus phonolite. Below this temperature, biotite would crystallize but it is not manifest in any Erebus lavas studied to date. Similarly, the lack of the amphibole–anorthoclase assemblage in Erebus' phonolitic products sets an upper limit on pressure of 200 MPa (Fig. 4a). The temperature of  $950 \pm 25^\circ\text{C}$  is somewhat lower than the previously reported temperature of the Erebus phonolite lava of 1000°C (Kyle, 1977; Caldwell & Kyle, 1994; Dunbar *et al.*, 1994) but it probably falls within the uncertainties of the pyrometric measurement. It is consistent, too, with the maximum surface temperature of 923°C measured by mid-infrared imaging of the lava lake (Calkins *et al.*, 2008). This measurement should represent a minimum for the melt temperature because it was made from the crater rim and has not accounted for the attenuation of radiation from the lake by the intervening gas plume-filled atmosphere. It must also under-represent the magmatic temperature because it is a measure of the surface temperature; that is, of the surface crust or skin, which will have cooled relative to magma beneath through radiative heat loss.

We emphasize that, considering the dry character of the system (see below), we can rule out temperatures much lower than 950°C in the shallow plumbing system, as they would drive the system toward much higher crystallinities than observed (i.e. closer to the solidus, as documented by the 0.1 MPa experiments, Table 2). High crystallinities would also inhibit the style of magma convection observed (Molina *et al.*, 2012). For instance, the 0.1 MPa charge at 925°C has nearly 70 wt % crystals (Table 2), which would increase magma viscosity by at least three orders of magnitude compared with that at 950°C (Champallier *et al.*, 2008). We note that the appearance of biotite at 925°C, almost irrespective of the water content, has been observed previously by Scaillet *et al.* (1995) for a peraluminous granite and by Bogaerts *et al.* (2006) for a metaluminous dacite.

As for the temperature of 1080°C reported by Burgisser *et al.* (2012) and used in their modelling of observed gas compositions for passive and explosive degassing from the lava lake, the discrepancy is substantial and, at this stage, we can only speculate on its cause. This high value was computed for ambient atmospheric pressure (in the Erebus crater, about 650 hPa) from equilibrium constants for the reaction



and field spectroscopic measurements of the abundances of each species. One possible scenario to explain why this procedure might overestimate the magmatic temperature is if the

measured SO<sub>2</sub> mass fraction in the gas plume is substantially higher than that in the magmatic gas. This could arise if H<sub>2</sub>S represents a significant part of the sulphur in the magmatic gas but is instantaneously oxidized to SO<sub>2</sub> on contact with air. In this case, the measured SO<sub>2</sub> in the plume would not reflect the gas phase equilibrium reached in the magma. Indeed, H<sub>2</sub>S has not been detected in the Erebus gas plume, despite the reduced magmatic conditions evident from the CO and H<sub>2</sub> content of the plume. But if this is correct, it remains a puzzle as to why H<sub>2</sub>S should oxidize in preference to CO and H<sub>2</sub>.

Isothermal phase-equilibrium experiments at a temperature of 950°C successfully reproduce the natural assemblage at all pressures below 200 MPa. Based on an average crustal density of 2.75 g cm<sup>-3</sup>, this is roughly equivalent to a depth of 7.5 km. As stated above, this should correspond to the maximum depth from which phonolite similar to that erupted in the lava lake could be sourced. Recent imaging of the conduit by means of seismic interferometry and seismic tomography (Chaput *et al.*, 2012; Zandomenighi *et al.*, 2013) has revealed a complex magmatic network within ~4 km of the surface, but did not identify any large magma reservoir. Considering the stability in the chemistry and phase assemblage of the phonolite erupted from Erebus over the last 20 kyr (Kelly *et al.*, 2008b) a large, well-mixed phonolitic reservoir is expected. Thus, this hypothetical reservoir should be located between 4 and 7.5 km depth.

The oxidation state imposed in the majority of experimental runs lies in the range QFM to QFM – 2, within which the Fe/Mg partition coefficient of experimental clinopyroxene–liquid pairs is very close, if not identical, to that recorded by the natural pair (Table 4). This argues consistently for oxygen fugacity conditions being in the same range for the natural system.

Isothermal and isobaric phase experiments have been carried out for a range of water contents. Whereas the natural assemblage stability window varies with pressure, the melt water contents must always remain below 0.5 wt %. At pressures lower than 100 MPa, for which our phase-equilibrium data are most detailed, melt water contents must be less than 0.25 wt %. These results are fully consistent with FTIR spectroscopic analyses of anorthoclase-hosted melt inclusions, whose dissolved water contents do not exceed 0.2 wt % (Eschenbacher, 1998; Oppenheimer *et al.*, 2011). Olivine-hosted melt inclusions from the parental basanite from which the Erebus phonolite is probably derived record H<sub>2</sub>O contents up to 1.75 wt % and up to 7000 ppm CO<sub>2</sub> (Oppenheimer *et al.* 2011). The dry character of the phonolitic system most probably reflects continuous fluxing by CO<sub>2</sub>-rich fluids coming from more primitive magmas at greater depth that desiccate the shallower fractionated melts (but maintaining them close to the liquidus owing to heat brought in by the incoming bubbles). This is a consequence of open-conduit conditions with a hot magmatic column that allows permanent circulation of CO<sub>2</sub>-rich bubbles because of the low viscosity of the melt. It also stems from the fact that deep bubbles are always richer in CO<sub>2</sub> than shallower ones, owing to the contrasting CO<sub>2</sub> and H<sub>2</sub>O solubilities. Hence deep-sourced and CO<sub>2</sub>-rich bubbles disconnect easily (because of low viscosity) from their magma source and rise, scavenging water from the shallower magma. A possible contributing factor is that H<sub>2</sub>O diffuses faster than CO<sub>2</sub>, hence rising bubbles will become selectively enriched in H<sub>2</sub>O relative to CO<sub>2</sub> owing to kinetic effects.

Possible evidence for H<sub>2</sub>O being drained out of the system can be inferred from surface measurements of gas emissions. Oppenheimer & Kyle (2008) reported on H<sub>2</sub>O flux of 10 kg s<sup>-1</sup> carried by the gas plume emitted from the lava lake. Taking an H<sub>2</sub>O content of 0.2 wt % in the melt would indicate a magma flux of 5000 kg s<sup>-1</sup>, or ~2 m<sup>3</sup> s<sup>-1</sup> of dense magma. This

estimate is a factor of five times higher than that estimated in the same fashion but based on the HCl emission rate and proportion of Cl exsolved from the melt. Although there are substantial uncertainties in these calculations, they tend to suggest that the H<sub>2</sub>O degassing at the surface cannot be accounted for solely by magma entering the lake; that is, some of the H<sub>2</sub>O has been sourced from deeper (un-erupted) magma, potentially scavenged from the melt by rising CO<sub>2</sub>-rich fluids.

### **Comparison with other phonolitic volcanoes**

To date, six phase-equilibrium studies of the pre-eruptive conditions of phonolite eruptions have been reported. The bulk compositions of these phonolites are variable: 51.3–60.3 wt % SiO<sub>2</sub>; 0.1–0.97 wt % TiO<sub>2</sub>; 18.77–22.80 wt % Al<sub>2</sub>O<sub>3</sub>; 1.80–4.50 wt % FeO<sub>T</sub>; 0.13–0.23 wt % MnO; 0.10–0.87 wt % MgO; 0.64–5.90 wt % CaO; 5.23–10.69 wt % Na<sub>2</sub>O; 5.17–10.20 wt % K<sub>2</sub>O; Na<sub>2</sub>O/K<sub>2</sub>O of 0.60–1.81. Accordingly, their associated phase stability diagrams differ markedly (see also Andújar & Scaillet, 2012).

Table 8 summarizes the pre-eruptive conditions identified through comparable experimental studies of phonolitic systems. Supplementary Data Fig. DR1 shows the variation in major oxides with respect to the determined eruption temperature for all phonolites studied to date. Figure DR1 shows, unsurprisingly, that higher eruption temperatures are associated with higher FeO<sub>T</sub>, MgO and TiO<sub>2</sub>, and lower K<sub>2</sub>O, SiO<sub>2</sub> and Al<sub>2</sub>O<sub>3</sub> contents. Na<sub>2</sub>O and CaO contents do not vary consistently with temperature. The higher temperature and hence lower viscosity of the Erebus phonolite, and to a lesser extent that of Tenerife, tends to favour effusive over explosive eruptions, such as typify Vesuvius and Laacher See. The higher temperature and lower viscosity at Erebus also helps to sustain an active lava lake by conduit convection (Molina *et al.*, 2012), probably driven by the density contrast of rising bubbly and volatile-rich magma and sinking degassed magma (e.g. Francis *et al.*, 1993; Kazahaya *et al.*, 1994). Although reported pressure ranges are comparable for all the phonolites examined, in comparison with other volcanoes, the phonolite erupted from Erebus is consistently and significantly hotter.

Table 8 : Comparison of pre-eruptive conditions determined for various phonolitic systems

Volcano or eruption:	Mercato	Avellino	Pompeii	Pollena	Laacher See	horizons			Kerguelen	Tenerife, Lavas Negras	Tenerife, El Abrigo	Erebus
Age:	8010 bp	3360 bp	ad 79	ad 472	LLST	MLST	ULST	Upper Miocene	1150 bp	190 ka	20 ka to present	
Temperature (°C)	785 ± 10	785 ± 10	815 ± 10	800 ± 10	720 ± 20	760–780	840–870	800	900 ± 20	825 ± 25	950 ± 25	
Pressure (kbar)	2 ± 0.2	2 ± 0.2	2 ± 0.2	1	2?	2?	2?	>2–2.5	1.5 ± 0.5	1.3 ± 0.5	<2	
wt % H <sub>2</sub> O	7 ± 0.5	5–5.5	6–6.5	3–4	?	>6	<6	4–6	2.5–3.5	3 ± 1	<0.5	
Oxidation state	NNO + 1	NNO + 1	NNO + 1	NNO + 1	NNO + 2?	NNO + 2?	NNO + 2?	NNO + 1 to NNO + 2	NNO + 1?	NNO ± 1	QFM to QFM – 1	
Reference	Scaillet <i>et al.</i> (2008)				Berndt <i>et al.</i> (2001)			Freise <i>et al.</i> (2003)	Andújar <i>et al.</i> (2009)	Andújar <i>et al.</i> (2008)	This study	

- Berndt *et al.* (2001) studied phonolite from the Laacher See tephra under conditions of 760–880°C, 200–400 MPa, NNO to NNO + 2.3, and 6–8 wt % H<sub>2</sub>O. Harms *et al.* (2004) studied similar tephra under more restricted conditions of 725–800°C, 750–1750 bar, NNO + 1 and uncertain H<sub>2</sub>O content. Freise *et al.* (2003) studied Upper Miocene phonolite lava from Kerguelen under conditions of 700–900°C, 100–500 MPa, NNO to NNO + 2.3 and 0.5–8 wt % H<sub>2</sub>O. Scaillet *et al.* (2008) studied four Vesuvius eruptions (Mercato, Avellino, Pompeii and Pollena) under conditions of 750–950°C, 50–350 MPa, NNO + 1 and 2–7.5 wt % H<sub>2</sub>O. Finally two experimental studies by Andújar *et al.* (2008) and Andújar *et al.* (2009) looked at the pre-eruptive conditions of the El Abrigo ignimbrite and Lavas Negras flow respectively, on Tenerife. Andújar *et al.* (2008) explored conditions of 700–900°C, 50–250 bar, NNO + 1 to QFM, and 1.5–10 wt % H<sub>2</sub>O. Andújar *et al.* (2009) looked at conditions of 750–925°C, 100–250 MPa, NNO + 1 and 1.3–10 wt % H<sub>2</sub>O.

Particularly striking compared with the other phonolitic systems, however, is the much lower water content for the Erebus phonolite and its distinctly more reduced character. These differences partly reflect the geodynamic setting of Erebus, located within a rift system above a hotspot, possibly a mantle plume (compare this situation with the subduction-related setting of some of the other phonolitic volcanoes considered). Another distinctive characteristic of the Erebus phonolite is its abundance of CO<sub>2</sub> (Eschenbacher, 1998; Oppenheimer *et al.*, 2011), compared with other phonolitic systems such as Vesuvius (Cioni, 2000). The continuous fluxing of the upper magmatic system by CO<sub>2</sub>-rich gas, promoted perhaps by the elevated temperature and lower melt viscosity, may provide a significant source of heat (e.g. Bachmann & Bergantz, 2003) and is thus an important contributing factor for maintaining isothermal conditions over long periods. CO<sub>2</sub> fluxing has also previously been hypothesized to occur beneath Stromboli (Allard, 2010) and Etna (e.g. Collins *et al.*, 2009). Within this context, it is also worth noting that, despite the continuous CO<sub>2</sub> flushing of the Erebus magma system and evidence for conduit convection and associated dynamical effects (Oppenheimer *et al.*, 2009, 2011), the crystal–melt equilibrium is fundamentally maintained in this system, as documented by the good agreement between our phase-equilibrium constraints and the main petrological attributes of the Erebus phonolite.

## Conclusions

We have constrained the conditions of the shallow plumbing system of Erebus volcano in  $P$ – $T$ – $H_2O$ – $fO_2$  space. The natural assemblage observed in the eruptive products has been successfully reproduced by phase-equilibrium experiments at a temperature of  $950 \pm 25^\circ\text{C}$ , and at pressures  $<200$  MPa. Recent seismological investigations appear to rule out the existence of any large magma reservoir shallower than 4 km, suggesting that if such a magma body exists it is located at a depth between 4 and 7.5 km, where it would have a water content  $<0.5$  wt % and an  $fO_2$  between QFM and QFM – 1. The temperature of the phonolitic lava or magma is  $\sim 50^\circ\text{C}$  lower than that previously accepted, which has significant implications for interpreting the composition of gases released from the lava lake, and for physical modelling of the magmatic system (e.g. melt viscosity would be approximately three times higher at  $950^\circ\text{C}$  than at  $1000^\circ\text{C}$ ). Compared with other phonolitic magmas, the Erebus phonolite is consistently drier, hotter and more reduced.

Taking into account the exceptional chemical and modal stability of the Erebus phonolite over the last 20 kyr (Kelly *et al.*, 2008b), the strong constraint we have imposed on the temperature of the lava to re-create the natural rock implies that the heat supply beneath the volcano must have remained extremely stable over this time period, never allowing the magma to cool below  $925^\circ\text{C}$ . Such thermal stability and evidence of  $\text{CO}_2$  fluxing argues for a plumbing system directly connected to the melting source region in the mantle, via one or several magma reservoirs (Oppenheimer *et al.*, 2011). Heat and fluid loss at the top of the system is constantly compensated by heat and fluid input from the source region preventing the shallow plumbing system from cooling over time.

## Funding

This research was supported by grants ANT0838817 and ANT1142083 from the Office of Polar Programs (National Science Foundation), and grant 202844 ('DEMONS') from the European Research Council (FP7). Y.M. was additionally supported by the University of Cambridge Home and EU Scholarship Scheme in addition to the Philip Lake and William Vaughan Lewis funds from the Department of Geography, University of Cambridge. C.O. also acknowledges support from the National Centre for Earth Observation (NERC NE/F001487/1 'Dynamic Earth and Geohazards' theme).

## Acknowledgements

We are very grateful to Joan Andújar, Rémi Champallier, Marina Alletti, Anita Cadoux, Mickael Laumonier, Giada Iacono Marziano, David Sifre, Nolwenn Le-gall, Fabrice Gaillard and Michel Pichavant for their help with various instruments and for inspiring discussions. Special thanks also go to Ida Di Carlo and Iris Buisman for invaluable help with the SEM and electron probe. We are also grateful to Marjorie Wilson, Ray Macdonald and an anonymous reviewer for their constructive reviews of the original work.

## References

- Andújar J, Scaillet B. *Relationships between pre-eruptive conditions and eruptive styles of phonolite–trachyte magmas. Lithos* 2012;152:122-131.
- Andújar J, Costa F, Martí J, Wolff J A, Carroll M R. *Experimental constraints on pre-eruptive conditions of phonolitic magma from the caldera-forming El Abrigo eruption, Tenerife (Canary Islands). Chemical Geology* 2008;257(3–4):173-191. doi:10.1016/j.chemgeo.2008.08.012.
- Andújar J, Costa F, Martí J. *Magma storage conditions of the last eruption of Teide volcano (Canary Islands, Spain). Bulletin of Volcanology* 2009;72(4):381-395. doi:10.1007/s00445-009-0325-3.
- Allard P. *A CO<sub>2</sub>-rich gas trigger of explosive paroxysms at Stromboli basaltic volcano, Italy. Journal of Volcanology and Geothermal Research* 2010;189(3–4):363-374.
- Aster R, Zandomenighi D, Mah S, McNamara S, Henderson D B, Knox H, Jones K. *Moment tensor inversion of very long period seismic signals from Strombolian eruptions of Erebus Volcano. Journal of Volcanology and Geothermal Research* 2008;177:635-647.
- Bachmann O, Bergantz G W. *Rejuvenation of the Fish Canyon magma body: a window into the evolution of large-volume silicic magma systems. Geology* 2003;31:789-792.
- Berndt J, Holtz F, Koepke J. *Experimental constraints on storage conditions in the chemically zoned phonolitic magma chamber of the Laacher See volcano. Contributions to Mineralogy and Petrology* 2001;140(4):469-486. doi:10.1007/PL00007674.
- Bogaerts M, Scaillet B, Vander Auwera J. *Phase equilibria of the Lyngdal Granodiorite (Norway): implications for the origin of oxidised A-type magmas. Journal of Petrology* 2006;12:2405-2431. doi:10.1093/petrology/egl049.
- Burgisser A, Oppenheimer C, Alletti M, Kyle P R. *Backward tracking of gas chemistry measurements at Erebus volcano. Geochemistry, Geophysics, Geosystems* 2012;12(11):Q11010. doi:10.1029/2012GC00424.
- Caldwell D, Kyle P R. *Mineralogy and geochemistry of ejecta erupted from Mount Erebus, Antarctica between 1972 and 1986. In: Kyle P R, editor. Volcanological and Environmental Studies of Mount Erebus. American Geophysical Union, Antarctic Research Series. Vol. 66. 1994. p. 147-162.*
- Calkins J, Oppenheimer C, Kyle P R. *Ground-based thermal imaging of lava lakes at Erebus volcano, Antarctica. Journal of Volcanology and Geothermal Research* 2008;177:695-704.
- Carroll M R, Blank J G. *The solubility of H<sub>2</sub>O in phonolitic melts. American Mineralogist* 1997;82:549-556.
- Champallier R, Bystricky M, Arbaret L. *Experimental investigation of magma rheology at 300 MPa: from pure hydrous melt to 76 vol. % of crystals. Earth and Planetary Science Letters* 2008;267:571-583.

Chaput J A, Zandomeneghi D, Aster R C, Knox H, Kyle P R. *Imaging of Erebus volcano using body wave seismic interferometry of Strombolian eruption coda. Geophysical Research Letters* 2012;39. doi:10.1029/2012GL050956.

Cioni R. *Volatile content and degassing processes in the AD 79 magma chamber at Vesuvius (Italy). Contributions to Mineralogy and Petrology* 2000;140:40-54.

Collins S J, Pyle D M, MacLennan J. *Melt inclusions track pre-eruption storage and dehydration of magmas at Etna. Geology* 2009;37(6):571-574.

Dall'Agnol R, Scaillet B, Pichavant M. *An experimental study of a lower Proterozoic A-type granite from the eastern Amazonian craton, Brazil. Journal of Petrology* 1999;40(11):1673-1698.

Devine J D, Gardner J E, Brack H P, Layne G D, Rutherford M J. *Comparison of microanalytical methods for estimating H<sub>2</sub>O contents of silicic volcanic glasses. American Mineralogist* 1995;80:319-328.

Di Carlo I, Pichavant M, Rotolo S G, Scaillet B. *Experimental crystallization of a high-K arc basalt: the Golden Pumice, Stromboli Volcano (Italy). Journal of Petrology* 2006;47(7):1317-1343.

Dunbar N W, Cashman K, Dupre R. *Crystallization processes of anorthoclase phenocrysts in the Mount Erebus magmatic system: evidence from crystal composition, crystal size distributions and volatile contents of melt inclusions. In: Kyle P R, editor. Volcanological and Environmental Studies of Mt. Erebus. American Geophysical Union, Antarctic Research Series. Vol. 66. 1994. p. 129-146.*

Eschenbacher A. 1998. *Open-system degassing of a fractionating, alkaline magma, Mount Erebus, Ross Island, Antarctica. Master's thesis, New Mexico Institute of Mining and Technology, Socorro.*

Esser R P, Kyle P R, McIntosh W C. *<sup>40</sup>Ar/<sup>39</sup>Ar dating of the eruptive history of Mount Erebus, Antarctica: volcano evolution. Bulletin of Volcanology* 2004;66:671-686.

Francis P W, Oppenheimer C, Stevenson D. *Endogenous growth of persistently active volcanoes. Nature* 1993;366:554-557.

Freise M, Holtz F, Scoates J, Leyrit H. *Experimental constraints on the storage conditions of phonolites from the Kerguelen Archipelago. Contributions to Mineralogy and Petrology* 2003;145(6):659-672. doi:10.1007/s00410-003-0453-2.

Gerst A, Hort M, Kyle P R, Voge M. *4D velocity of Strombolian eruptions and man-made explosions derived from multiple Doppler radar instruments. Journal of Volcanology and Geothermal Research* 2008;177:648-660.

Gerst A, Horst M, Aster R, Johnson J, Kyle P R. *The first second of a Strombolian volcanic eruption - Energies, pressures, infrasound. Journal of Geophysical Research* 2013. (in review).

Gupta S, Zhao D P, Rai S S. *Seismic imaging of the upper mantle under the Erebus hotspot in Antarctica. Gondwana Research* 2009;16:109-118.

Harms E, Gardner J E, Schmincke H-U. *Phase equilibria of the Lower Laacher See Tephra (East Eifel, Germany): constraints on pre-eruptive storage conditions of a phonolitic magma reservoir. Journal of Volcanology and Geothermal Research* 2004;134(1-2):125-138.

Harpel C J, Kyle P R, Esser R P, McIntosh W C, Caldwell D A.  $^{40}\text{Ar}/^{39}\text{Ar}$  dating of the eruptive history of Mount Erebus, Antarctica: summit flows, tephra, and caldera collapse. *Bulletin of Volcanology* 2004;66:687-702.

Harpel C J, Kyle P R, Dunbar N W. *Englacial tephrostratigraphy of Erebus volcano, Antarctica. Journal of Volcanology and Geothermal Research* 2008;177:549-568.

Kazahaya K, Shinohara H, Saito G. *Excessive degassing of Izu-Oshima volcano: magma convection in a conduit. Bulletin of Volcanology* 1994;56:207-216.

Kelly P, Dunbar N, Kyle P, McIntosh W. *Refinement of the late Quaternary geologic history of Erebus volcano, Antarctica using  $^{40}\text{Ar}/^{39}\text{Ar}$  and  $^{36}\text{Cl}$  age determinations. Journal of Volcanology and Geothermal Research* 2008a;177:569-577.

Kelly P J, Kyle P R, Dunbar N W, Sims K W W. *Geochemistry and mineralogy of the phonolite lava lake, Erebus volcano, Antarctica: 1972–2004 and comparison with older lavas. Journal of Volcanology and Geothermal Research* 2008b;177:589-605.

Kyle P R. *Mineralogy and glass chemistry of recent volcanic ejecta from Mt. Erebus, Ross Island, Antarctica. New Zealand Journal of Geology* 1977;20:1123-1146.

Kyle P R. *McMurdo Volcanic Group Western Ross Embayment: Introduction. In: LeMasurier W, Thompson J, editors. Volcanism of the Antarctic Plate and Southern Oceans. 1990a. Antarctic Research Series, Vol. 48. American Geophysical Union, pp. 18–25.*

Kyle P R. *Erebus volcanic Province: Summary. In: LeMasurier W, Thompson J, editors. Volcanism of the Antarctic Plate and Southern Oceans. 1990b. Antarctic Research Series, Vol. 48. American Geophysical Union, pp. 81–88.*

Kyle P, Dibble R, Giggenbach W, Keys J. *Volcanic activity associated with the anorthoclase phonolite lava lake, Mt. Erebus, Antarctica. In: Craddock C, editor. Antarctic Geosciences. Madison, WI: University of Wisconsin Press; 1982. p. 735-745.*

Kyle P R, Moore J A, Thirlwall M F. *Petrologic evolution of anorthoclase phonolite lavas at Mount Erebus, Ross Island, Antarctica. Journal of Petrology* 1992;33:849-875.

Kyle P R, Sybeldon L M, McIntosh W C, Meeker K, Symonds R. *Sulfur dioxide emission rates from Mount Erebus, Antarctica. In: Kyle P R, editor. Volcanological and Environmental Studies of Mount Erebus. American Geophysical Union, Antarctic Research Series. Vol. 66. 1994. p. 69-82.*

Le Bas M J, Lemaître R W, Streckeisen A, Zanettin B. *A chemical classification of volcanic rocks based on the total alkali–silica diagram. Journal of Petrology* 1986;27(3):745-750.

- Molina I, Burgisser A, Oppenheimer C. *Origin of steady convection in Erebus lava lake, Antarctica: The effects of crystals in open and closed systems. Journal of Geophysical Research* 2012.
- Moussallam Y, Oppenheimer C, Aiuppa A, Giudice G, Moussallam M, Kyle P. *Hydrogen emissions from Erebus volcano, Antarctica. Bulletin of Volcanology* 2012;74(9):2109-2120.
- Oppenheimer C, Kyle P R. *Probing the magma plumbing of Erebus volcano, Antarctica, by open-path FTIR spectroscopy of gas emissions. Journal of Volcanology and Geothermal Research* 2008;177:743-754.
- Oppenheimer C, Lomakina A S, Kyle P R, Kingsbury N G, Boichu M. *Pulsatory magma supply to a phonolite lava lake. Earth and Planetary Science Letters* 2009;284:392-398.
- Oppenheimer C, Moretti R, Kyle P R, Eschenbacher A, Lowenstern J B, Hervig R L, Dunbar N W. *Mantle to surface degassing of alkalic magmas at Erebus volcano, Antarctica. Earth and Planetary Science Letters* 2011;306:261-271. doi:10.1016/j.epsl.2011.04.005.
- Prouteau G, Scaillet B. *Experimental constraints on the origin of the 1991 Pinatubo dacite. Journal of Petrology* 2003;44(12):2203-2241.
- Scaillet B, Pichavant M, Roux J, Humbert G, Lefèvre A. *Improvement of the Shaw membrane technique for measurement and control of  $f_{H_2}$  at high temperatures and pressures. American Mineralogist* 1992;77:647-655.
- Scaillet B, Pichavant M, Roux J. *Experimental crystallization of leucogranite magmas. Journal of Petrology* 1995;36(3):663-705.
- Scaillet B, Pichavant M, Cioni R. *Upward migration of Vesuvius magma chamber over the past 20,000 years. Nature* 2008;455(7210):216-219. doi:10.1038/nature07232.
- Schmidt B C, Behrens H. *Water solubility in phonolite melts: Influence of melt composition and temperature. Chemical Geology* 2008;256(3-4):259-268.
- Taylor J R, Wall V J, Pownceby M I. *The calibration and application of accurate redox sensors. American Mineralogist* 1992;77:284-295.
- Zandomenighi D, Aster R, Kyle P R, Barclay A, Chaput J, Knox H. *Internal structure of Erebus volcano, Antarctica imaged by high-resolution active-source seismic tomography and coda interferometry. Journal of Geophysical Research* 2013;118:1067-1078.